Supplementary Information

Addressing Ambient Stability Challenges in Pure FASnI3 Perovskite Solar Cells Through Organic Additives Engineering

Sergio Galve-Lahoz,[1,2] Jesús Sánchez-Diaz,[1] Carlos Echeverría-Arrondo,[1,3] Jorge Simancas,[1] Jhonatan Rodriguez-Pereira,[4,5] Silver-Hamill Turren-Cruz,[1,6] Juan P. Martinez-Pastor,[6] Iván Mora-Seró[1] and Juan Luis Delgado,[2,7*]*

[1] Institute of Advanced Materials (INAM), University Jaume I, Av. Vicent Sos Baynat, s/n, 12071, Castellón de la Plana, Spain

[2] Polymat, University of the Basque Country UPV/EHU, 20018 Donostia-San Sebastian, Spain.

[3] Institute of Chemical Research of Catalonia (ICIQ), Avda. Països Catalans 16, 43007 Tarragona (Spain)

[4] Center of Materials and Nanotechnologies, Faculty of Chemical Technology, University of Pardubice, nám. Cs. legií 565, Pardubice, 53002, Czech Republic

[5] Central European Institute of Technology, Brno University of Technology, Purkynova 123, Brno, 612 00, Czech Republic

[6] Instituto de Ciencia de los Materiales (ICMUV), Universitat de Valencia, 46980 Paterna, Spain

[7] Ikerbasque, Basque Foundation for Science, Bilbao 48013, Spain

*Corresponding authors: sero@uji.es, juanluis.delgado@polymat.eu

Materials

Chemicals and solvents were purchased from Sigma-Aldrich and Acros Organics, and used as received without further purification. Anhydrous solvents were dried using a Pure Solve solvent purification system. Column chromatography was performed using silica gel (40 to 60 µm, Acros Organics) from Fisher as the stationary phase, and thin layer chromatography (TLC) was conducted on pre-coated silica gel. The materials used in the photovoltaic study were obtained from commercial suppliers in high purity and employed without further purification: Formamidinium iodide (FAI, 99.99%) was purchased from Greatcell Solar Materials. C60 (99.95%) was obtained from Nano-C. Tin (II) iodide (SnI_2, 99.99%), tin (II) fluoride (SnF_2, 99%), bathocuproine (BCP, 99.99%), N,N-dimethylformamide (DMF, 99.8%), dimethylsulfoxide (DMSO, 99.8%) were purchased from Sigma-Aldrich. PEDOT:PSS Al 4083 aqueous solution was purchased from Heraeus.

Device fabrication

2.5 x 2.5 cm pre-patterned ITO substrates were washed in subsequent ultrasonic baths for 15 minutes each. First, the substrates were washed with water and soap and rinsed with mili-Q water. Then, the substrates were washed with ethanol, acetone and isopropanol and finally dried with N_2 flow and cleaned with an UV-Ozone lamp for 15 minutes just before the hole transport material (HTM). For the deposition of the HTM, a PEDOT:PSS solution was filtered with 0.45 µm PVDF filter and spin-coated on top of ITO at 3500 rpm (3500 rpm·s^{-1}) for 40 s and then annealed at 125°C for 30 minutes. After the deposition of the HTM, the substrates were introduced to a N_2-filled glovebox for the $FASnI_3$ layer deposition (FA, formamidinium). The $FASnI_3$ solution (0.9 M in 9:1 DMSO:DMF, with 10% SnF_2) was spin-coated on top of PEDOT:PSS at 4000 rpm for 50s. After 27 seconds of spinning, 350 µL of chlorobenzene with or without **OM4** or **OM6** 0.40 mM and AIBN 0.04 mM were dropped on the substrate to induce perovskite

crystallization, followed by a two-step annealing at 70°C for 1 minute and 100°C for 20 minutes. As an electron transport layer, 30 nm of C_{60} were thermally evaporated on top of the perovskite layer, followed by 6 nm of BCP as a buffer layer and 100 nm of Ag as metal contact. Finally, a three-day light soaking treatment was performed as part of device fabrication.[1]

Molecular characterization

Nuclear magnetic resonance (NMR) spectroscopy

All the NMR spectra were recorded on a Bruker Advance 300 (300 MHz for ^{1}H NMR; 75 MHz for ^{13}C NMR and 376 MHz for ^{19}F NMR) spectrometer at 298 K and referenced to deuterated solvent (e.g., CHCl3-d corrected to 7.26 and 77.16 ppm; DCM-d2 to 5.32 and 54.00 ppm; DMSO-d6 to 2.50 and 39.52 ppm for ^{1}H and ^{13}C NMR spectra, respectively). Coupling constants (J) are given in Hz and chemical shifts (δ) are reported in ppm. Multiplicities are denoted as follows: s (singlet), d (doublet), t (triplet), q (quartet), dd (doublet of doublets), m (multiplet), br s (broad singlet), br m (broad multiplet).

Mass spectrometry

High-Resolution Matrix-Assisted Laser Desorption Ionization, coupled to a Time-Of-Flight (TOF) analyzer experiments (MALDI-TOF) were carried out on a Bruker Ultraflex III spectrometer. All data were recorded at a maximum accelerating potential of 20 kV in the linear negative ion mode. DCTB was used as a matrix and AgTFA was added as the cationic ionization agent.

Structural characterization

X-ray diffraction (XRD)

XRD patterns of the films were measured using a powder X-ray diffractometer (D8 Advance, Bruker-AXS) in a Bragg-Bretano geometry, using Cu K_α X-ray radiation (λ_1 = 1.5406 Å, λ_2 = 1.5444 Å, I_2/I_1 = 0.5), with a tube voltage and intensity of 40 kV and 40 mA, respectively. The goniometer arm length was 217.5 mm, using a divergence slit fixed at 0.6º. The detector was a BRUKER-binary V3, using a scan range from 5.0º to 70.0º (2θ º), with a scan step size of 0.02 (2θ º) and a counting time of 75 s/step. Measurements were registered at room temperature (298 K).

Scanning Electron Microscope (SEM)

The topographical and cross-sectional images were taken using a field emission scanning electron microscope (FEG-SEM) JEOL 3100F operated at 15 kV. The SEM images were recorded from films deposited on top of ITO covered substrates.

X-ray Photoelectron Spectroscopy (XPS)

The surface chemical composition and electronic state of perovskites films with and without OM4 and OM6 were determined by XPS (ESCA-2SR, Scienta-Omicron). Spectra were recorded using monochromatic Al Kα = 1486.6 eV operated at 200W. The charge was controlled with the charge neutralizer (CN-10) operated at 5μA and 2eV. The binding energy scale was referenced to adventitious carbon (284.8 eV). CasaXPS processing software (Casa software Ltd) was used to analyze the data and the quantitative analysis was made using sensitivity factors provided by the manufacturer.

Water contact angle

The water contact angle was measured using a Kruss DSA25E Drop Shape Analyzer by dropping a droplet of deionized water onto the different substrates. A 30-seconds video was recorded

registering the behavior of the drop until its stabilization and the contact angle of the stable drop was measured using the DSA25E built-in software.

Optoelectronic characterization

UV-Vis Spectra

The absorption spectra were recorded using a Varian Cary 300 UV/Vis absorption spectrophotometer. UV-Vis spectra were obtained from films deposited on top of glass substrates.

Steady-state Photoluminescence (PL) and Time-Resolved PL (TRPL)

The PL and TRPL characterization of the different fabricated samples was carried out at room temperature and vacuum conditions, in order to avoid any oxidation effect during the measurements and hence having identical conditions for all samples (that were conveniently packed inside the glove box where they were prepared). The characterization was performed in a 90o excitation-detection backscattering configuration using a high-resolution Edinburgh FLS1000 system using an excitation wavelength of 465 nm produced by a Xe lamp for PL or a supercontinuum pulsed laser (FYLA SCT1000) for TRPL, both filtered by the excitation double monochromator. The detection for both PL and TRPL was performed with a cooled near-infrared photomultiplier (Hamamatsu H10330-75). The overall time resolution was in the range of 0.3-0.4 ns, because any deconvolution was applied for extracting the characteristic decay times.

Solar Cell Performance Measurement

The current density -voltage (J-V) curves were measured using an Abet technologies (Sun, 2,000) solar simulator. The light intensity was adjusted to 1 sun (100 $mW \cdot cm^{-2}$) using a calibrated Si solar cell and a photodiode The devices were measured in ambient conditions and without encapsulation. The active area of the cell is defined with a 0.121 cm^2 mask.

Computational details and results

We computed bulk $FASnI_3$ matrix in the orthorhombic Amm2 phase, as derived from XRD analysis, and extracted the lattice parameters: a= 6,448 Å; b= 8.718 Å; c= 8.919 Å. From these lattice values, we built up slabs with (001) surface orientation and the most stable SnI_2 termination. On these slabs, we included relevant defect species in Sn-based perovskites,[2] namely V_{Sn} and Sn_I, and both **OM4** and **OM6** adsorbed species; their atomic structures are illustrated in **Figure S28**. All these geometries were optimized with the VASP code[3-6] at the PBE level of theory[7] on the Γ point, until a threshold value for the forces of 0.05 eV/Å. We used dispersion corrections,[8] a cutoff energy for the plane-wave basis set of 500 eV, and a vacuum separation between adjacent layers of 8 Å.

*Synthesis of **OM4** and **OM6***

The synthesis of **OM4** and **OM6** are depicted in **Schemes S1** and **S2**. All the details and spectroscopy data are described below.

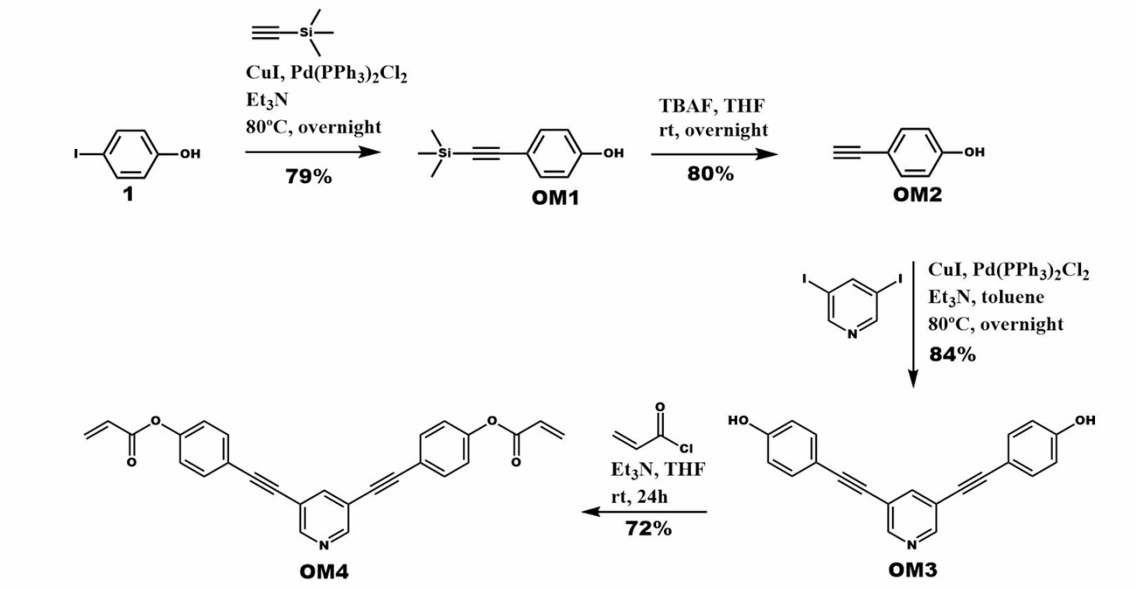

Scheme S1. Synthetic route for **OM4**.

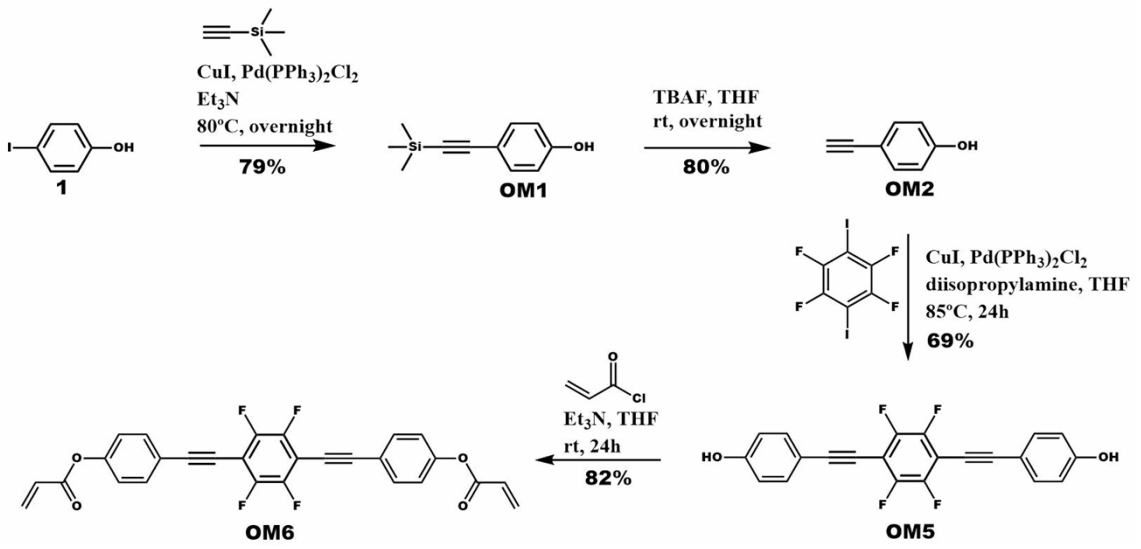

Scheme S2. Synthetic route for **OM6**.

4-[2-(Trimethylsilyl)ethynyl]phenol (OM1)

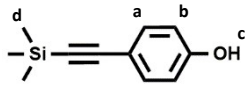

Ethynyltrimethylsilane (0.93 mL, 6.72 mmol) was added to a solution of 4-iodophenol (**1** ,4.64 mmol, 1.02 g), $Pd(PPh_3)_2Cl_2$ (98.26 mg, 0.14 mmol) and CuI (26.63 mg, 0.14 mmol) in 15 mL Et_3N and the mixture was refluxed at 80°C overnight under nitrogen atmosphere. The solution was then cooled to room temperature and concentrated under reduced pressure and the resulting residue was purified by flash column chromatography using Hexane/EtOAc as eluent to give the final compound as a white powder (700 mg, 79%). MS (MALDI-TOF): calculated for $C_{11}H_{14}OSi$ [M+H$^+$]: 191.10, found: 191.08. ^{1}H NMR (300 MHz, $CDCl_3$), δ (ppm): 7.36-7.33 (m, 2H, H_a), 6.75-6.72 (m, 2H, H_b), 4.91 (s, 1H, H_c), 0.22 (s, 9H, H_d) ^{13}C NMR (75 MHz, ($CDCl_3$) δ (ppm): 156.23, 133.79, 115.55, 105.52, 92.59, 61.28, 0.15.

4-ethynylphenol (OM2):

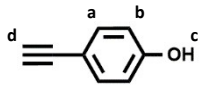

4-[2-(Trimethylsilyl)ethynyl]phenol (0.5 g, 2.6 mmol) was dissolved in dry THF (10 mL) and 3.12 mL of TBAF sol. 1 M in THF (1.2 eq) were added dropwise at room temperature. The resulting solution was stirred for 3 hours. The reaction was then quenched with saturated aqueous NH_4Cl solution and the mixture extracted with EtOAc. The organic layer was washed with water and brine. After drying over $MgSO_4$ and evaporating the solvent, the crude product was purified by flash column chromatography using Hexane/EtOAc as eluent to give the corresponding final product as a red oil (0.24 g, 80%). ^{1}H NMR (300 MHz, $CDCl_3$) δ (ppm): 7.40-7.37 (m, 2H, H_a), 6.79-6.76 (m, 2H, H_b), 5.32 (s, 1H, H_c), 2.98 (s, 1H, H_d).

4,4'-(pyridine-3,5-diylbis(ethyne-2,1-diyl))diphenol (OM3):

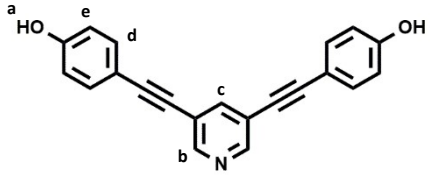

3,5-Diiodo pyridine (100 mg, 0.30 mmol), $PdCl_2(PPh_3)_2$ (21.06 mg, 0.03 mmol) and CuI (5.71 mg, 0.03 mmol) were dissolved in the minimum amount of toluene (60 mL). Et_3N (20 mL) and **OM2** (74.36 mg, 0.63 mmol) were then added and the reaction mixture was heated at 80°C overnight. The solvent was removed and the product crude dissolved in EtOAc and washed with water and brine. The organic phase was dried over $MgSO_4$ and the solvent removed under reduced pressure. The crude product was purified by flash column chromatography using Hexane/EtOAc as eluent to give the corresponding final product as a white powder (78.70 mg, 84%). MS (MALDI-TOF): calculated for $C_{21}H_{13}NO_2$ [M+H$^+$]: 312.34, found: 312.10. ^{1}H NMR (300 MHz, Acetone-d_6), δ (ppm): 8.92 (s, 2H, H_a), 8.64 (d, 2H, H_b), 7.95 (s, 1H, H_c), 7.49-7.46 (m, 4H, H_d), 6.94-6.91 (m, 4H, H_e) ^{13}C NMR (75 MHz, Acetone-d_6) δ (ppm): 160.08, 151.54, 141.07, 134.94, 122.06, 117.30, 114.53, 95.11, 84.87

4,4'-((perfluoro-1,4-phenylene)bis(ethyne-2,1-diyl))diphenol (OM5):

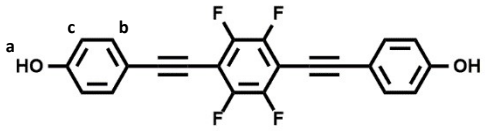

1,2,4,5-tetrafluoro-3,6-diiodobenzene (100 mg, 0.24 mmol), $PdCl_2(PPh_3)_2$ (21.06 mg, 0.03 mmol) and CuI (5.71 mg, 0.03 mmol) were dissolved in 40 mL of THF. Subsequently, 20 mL of diisopropylamine and **OM2** (59.42 mg, 0.50 mmol) were added and the reaction mixture was heated at 85°C for 24h. The solvent was removed and the product crude dissolved in EtOAc and washed with water and brine. The organic phase was dried over $MgSO_4$ and the solvent removed under reduced pressure. The crude product was purified by flash column chromatography using

Hexane/EtOAc as eluent to give the corresponding final product as a white powder (51.72 mg, 69%). MS (MALDI-TOF): calculated for $C_{22}H_{10}F_4O_2$ [M+H$^+$]: 382.06, found: 382.31. ^{1}H NMR (300 MHz, Acetone-d_6), δ (ppm): 8.95 (s, 2H, H_a), 7.43-7.40 (m, 4H, H_c), 6.89-6.86 (m, 4H, H_b) ^{13}C NMR (75 MHz, Acetone-d_6) δ (ppm): 159.66, 134.95, 134.59, 116.88, 116.70, 113.13, 82.11, 73.14

(pyridine-3,5-diylbis(ethyne-2,1-diyl))bis(4,1-phenylene) diacrylate (OM4):

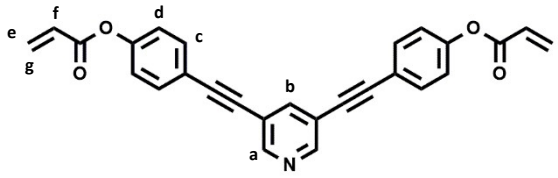

50 mg of **OM3** were dissolved in THF and triethylamine (29.34 mg, 0.29 mmol) was added. Acryloyl chloride (25.96 mg, 0.29 mmol) was added dropwise via syringe under a nitrogen atmosphere at room temperature. The reaction mixture was quenched after 24 h with saturated aqueous $NaHCO_3$, (30 mL) and transferred to a separating funnel. The final mixture was washed with saturated aqueous $NaHCO_3$, and water before being dried with $MgSO_4$, and then concentrated under reduced pressure. The crude product was purified by column chromatography using Hexane/EtOAC as eluent to give the final product as a yellow powder (48,46 mg, 72%). MS (MALDI-TOF): calculated for $C_{27}H_{17}NO_4$ [M+H$^+$]: 420.44, found: 420.11. ^{1}H NMR (300 MHz, $CDCl_3$), δ (ppm): 8.68 (s, 2H, H_a), 7.93 (s, 1H, H_b), 7.59-7.56 (m, 4H, H_c), 7.19-7.16 (m, 4H, H_d), 6.66-6.60 (dd, 2H, H_e), 6.37-6.28 (q, 2H, H_f), 6.06-6.02 (dd, 2H, H_g) ^{13}C NMR (75 MHz, $CDCl_3$) δ (ppm): 164.27, 151.09, 150.96, 140.71, 133.21, 133.11, 127.79, 122.00, 120.12, 92.62, 85.44

((perfluoro-1,4-phenylene)bis(ethyne-2,1-diyl))bis(4,1-phenylene) diacrylate (OM6):

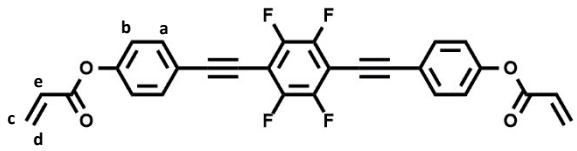

50 mg of **OM5** were dissolved in THF and triethylamine (27.51 mg, 0.27 mmol) was added. Acryloyl chloride (24.30 mg, 0.27 mmol) was added dropwise via syringe under a nitrogen atmosphere at room temperature. The reaction mixture was quenched after 24 h with saturated aqueous $NaHCO_3$, and transferred to a separating funnel. The final mixture was washed with saturated aqueous $NaHCO_3$, and water before being dried with $MgSO_4$, and then concentrated under reduced pressure. The crude product was purified by column chromatography using Hexane/EtOAC as eluent to give the final product as a white powder (52,74 mg, 82%). MS (MALDI-TOF): calculated for $C_{28}H_{14}F_4O_4$ [M+H$^+$]: 491.41, found: 491.13. 1H NMR (300 MHz, $CDCl_3$), δ (ppm): 7.65-7.62 (m, 4H, H_a), 7.21-7.19 (m, 4H, H_b), 6.67-6.61 (dd, 2H, H_c), 6.38-6.28 (q, 2H, H_d), 6.07-6.03 (dd, 2H, H_e) 13C NMR (75 MHz, CDCl3) δ (ppm): 164.77, 151.83, 134.91, 134.46, 133.83, 128.29, 122.55, 120.09, 116.34, 81.51, 74.67

OM1 (^{1}H NMR, 300 MHz, $CDCl_3$, 298K)

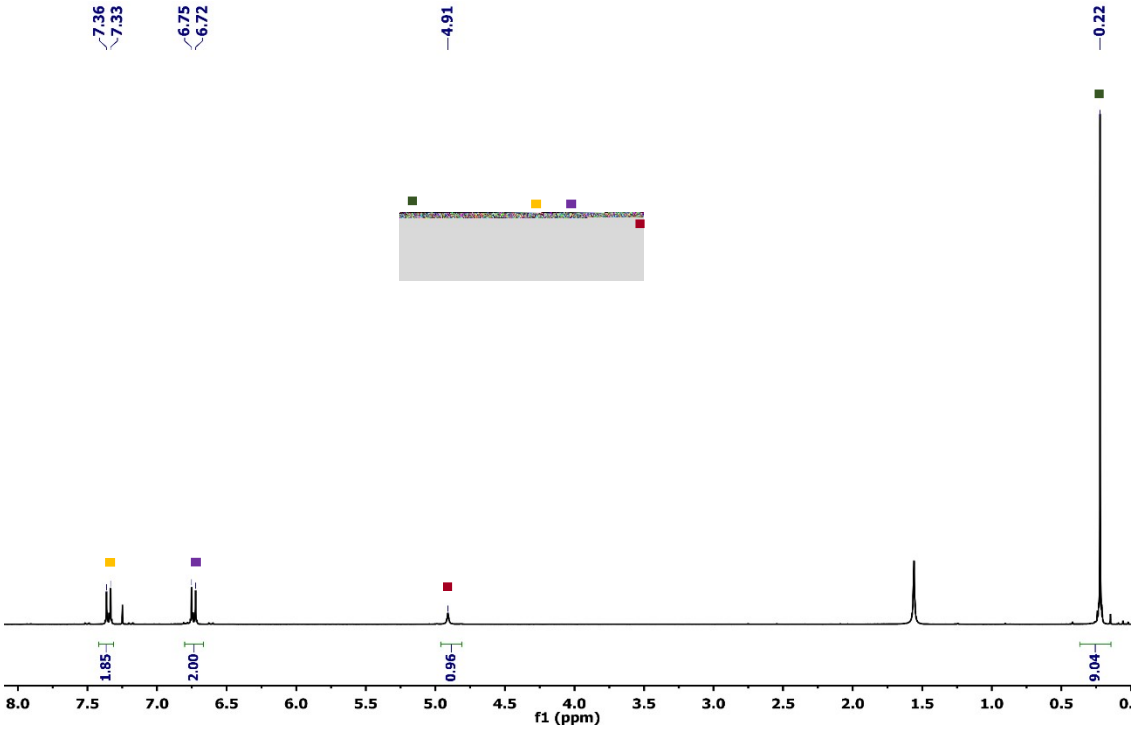

Figure S1. ^{1}H NMR spectrum (300 MHz, $CDCl_3$, 298K) of **OM1**

OM1 (^{13}C NMR, 300 MHz, $CDCl_3$, 298K)

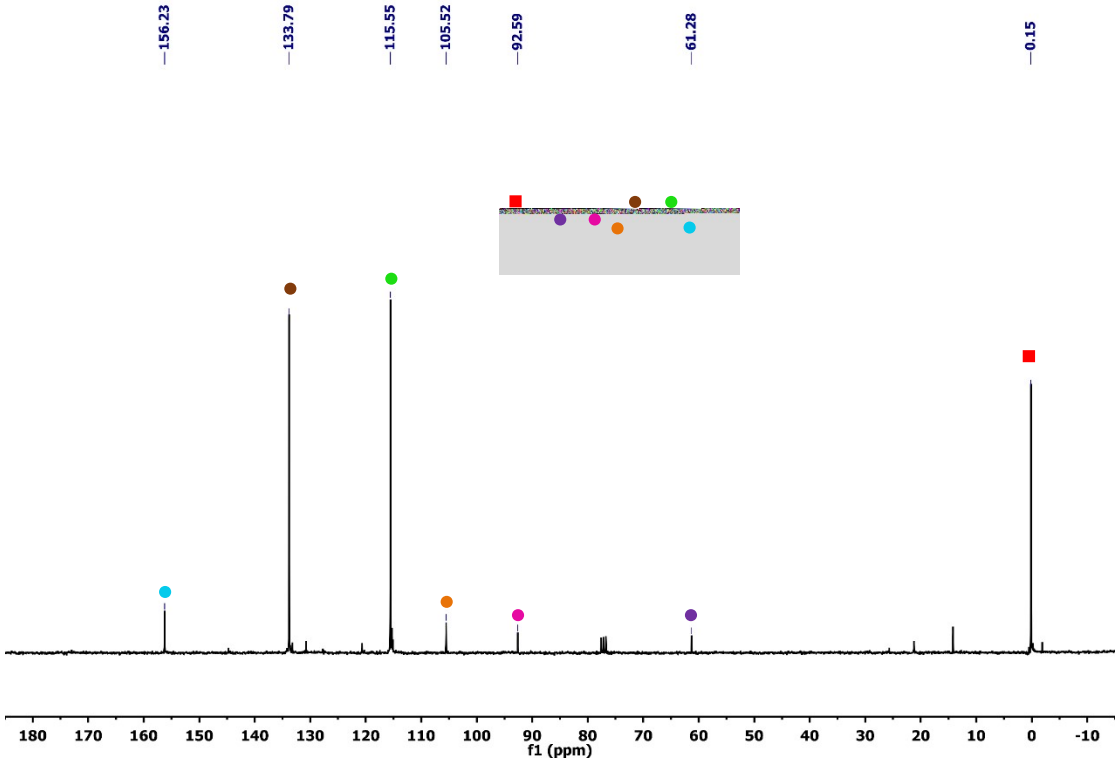

Figure S2. ^{13}C NMR spectrum (300 MHz, $CDCl_3$, 298K) of **OM1**

OM2 (^{1}H NMR, 300 MHz, $CDCl_3$, 298K)

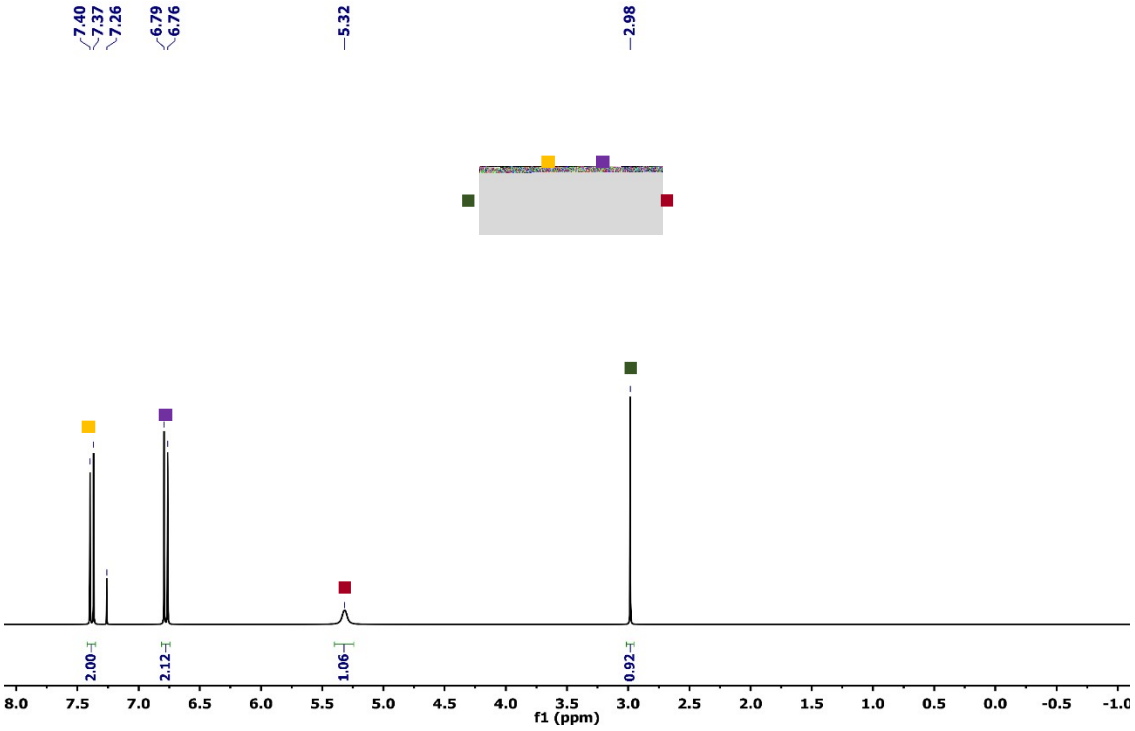

Figure S3. ^{1}H NMR spectrum (300 MHz, $CDCl_3$, 298K) of **OM2**

OM3 (^{1}H NMR, 300 MHz, $CDCl_3$, 298K)

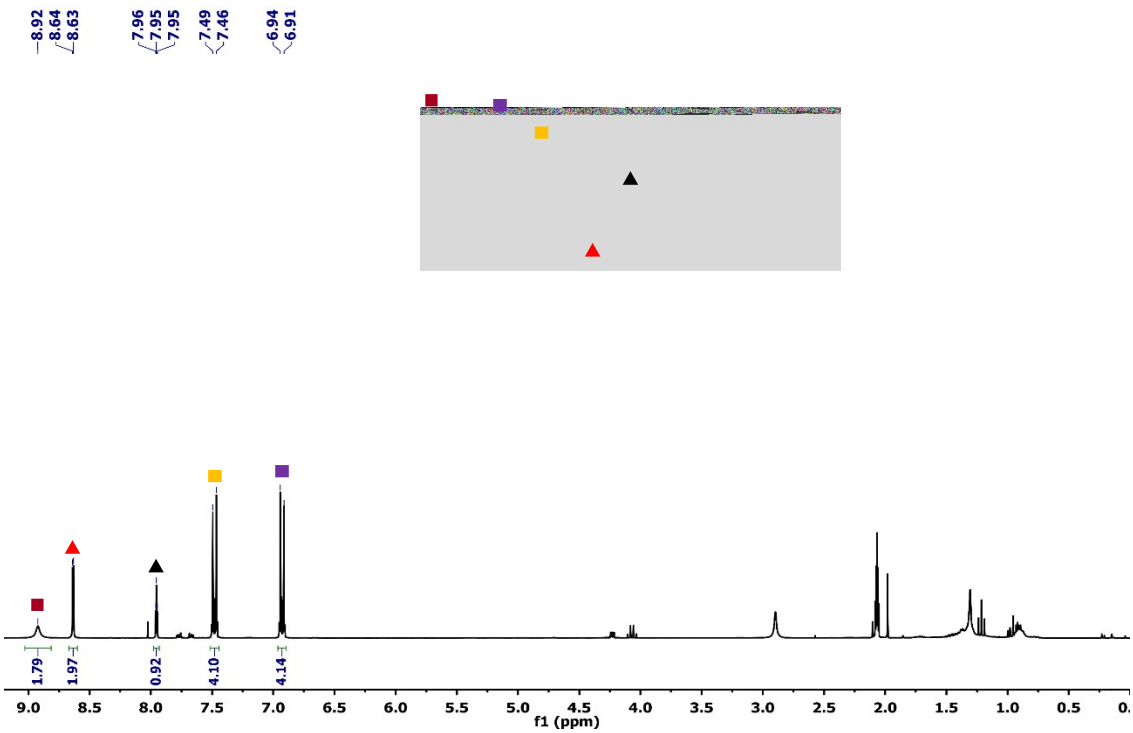

Figure S4. ^{1}H NMR spectrum (300 MHz, $CDCl_3$, 298K) of **OM3**

OM3 (^{13}C NMR, 300 MHz, $CDCl_3$, 298K)

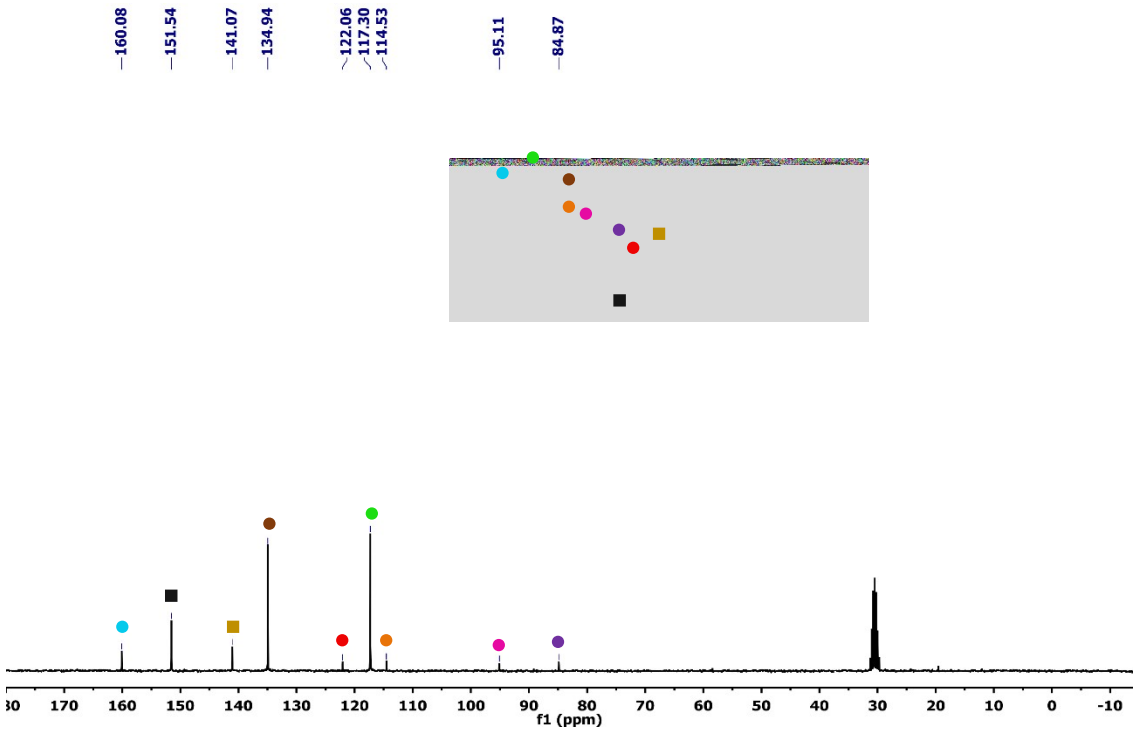

Figure S5. ^{13}C NMR spectrum (300 MHz, $CDCl_3$, 298K) of **OM3**

OM4 (^{1}H NMR, 300 MHz, $CDCl_3$, 298K)

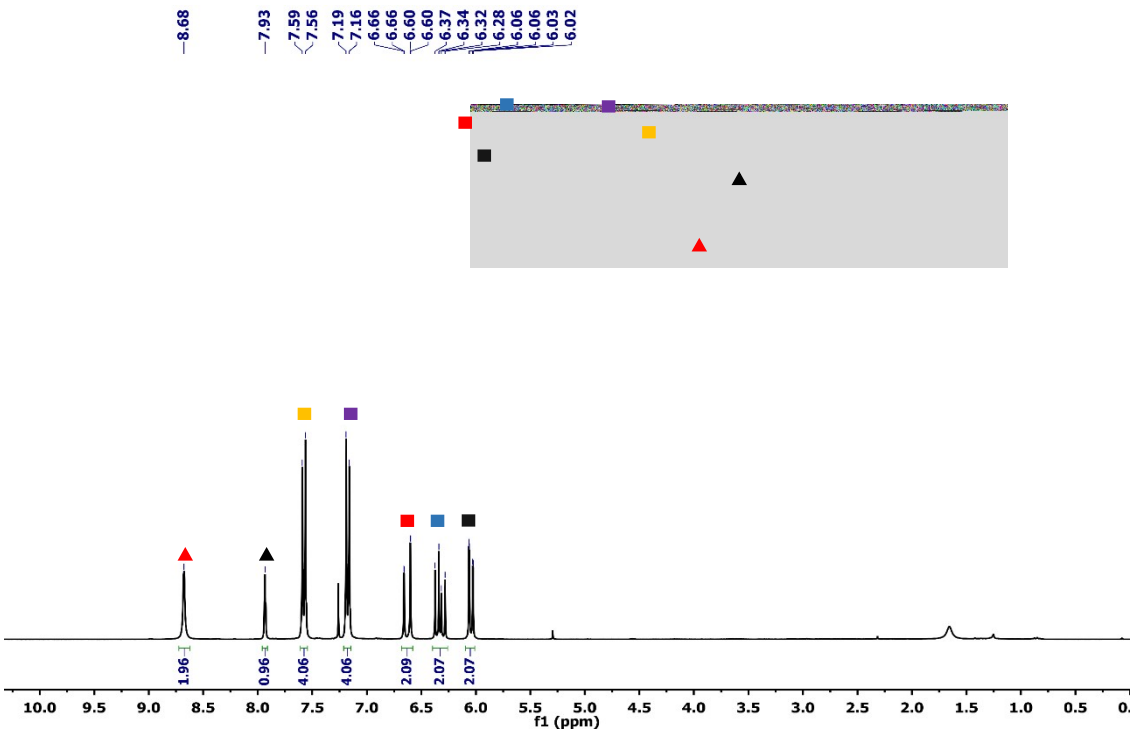

Figure S6. ^{1}H NMR spectrum (300 MHz, $CDCl_3$, 298K) of **OM4**

OM4 (^{13}C NMR, 300 MHz, $CDCl_3$, 298K)

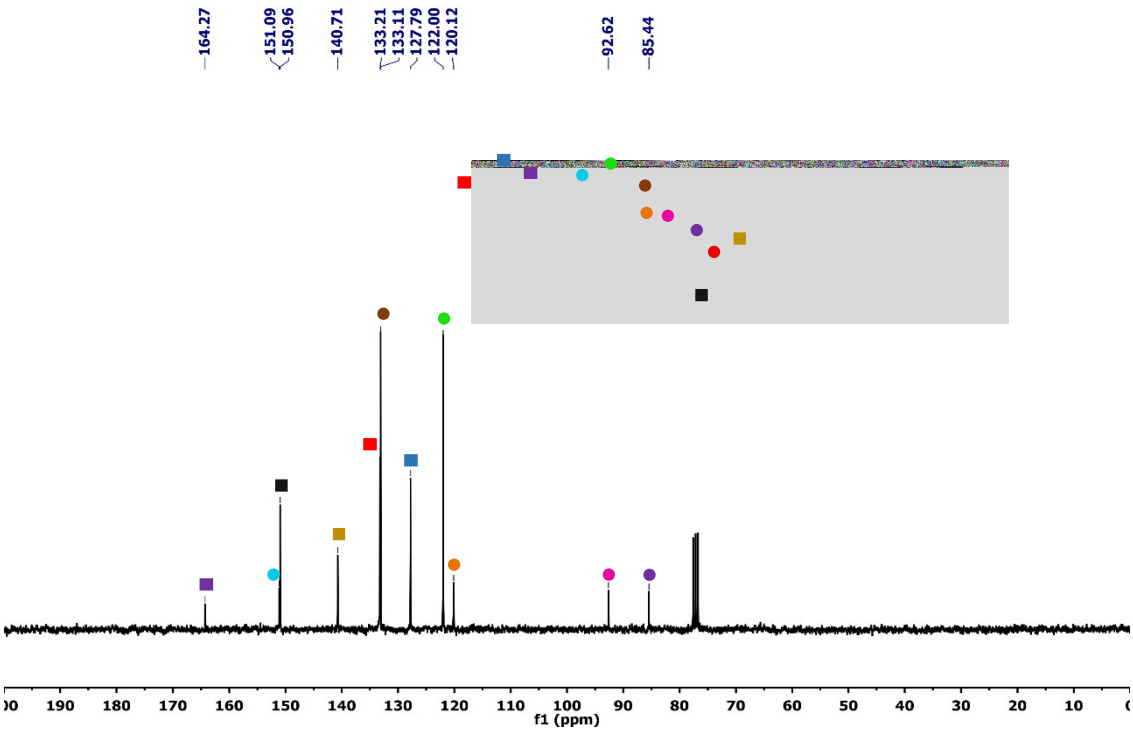

Figure S7. ^{13}C NMR spectrum (300 MHz, $CDCl_3$, 298K) of **OM4**

OM5 (^{1}H NMR, 300 MHz, $CDCl_3$, 298K)

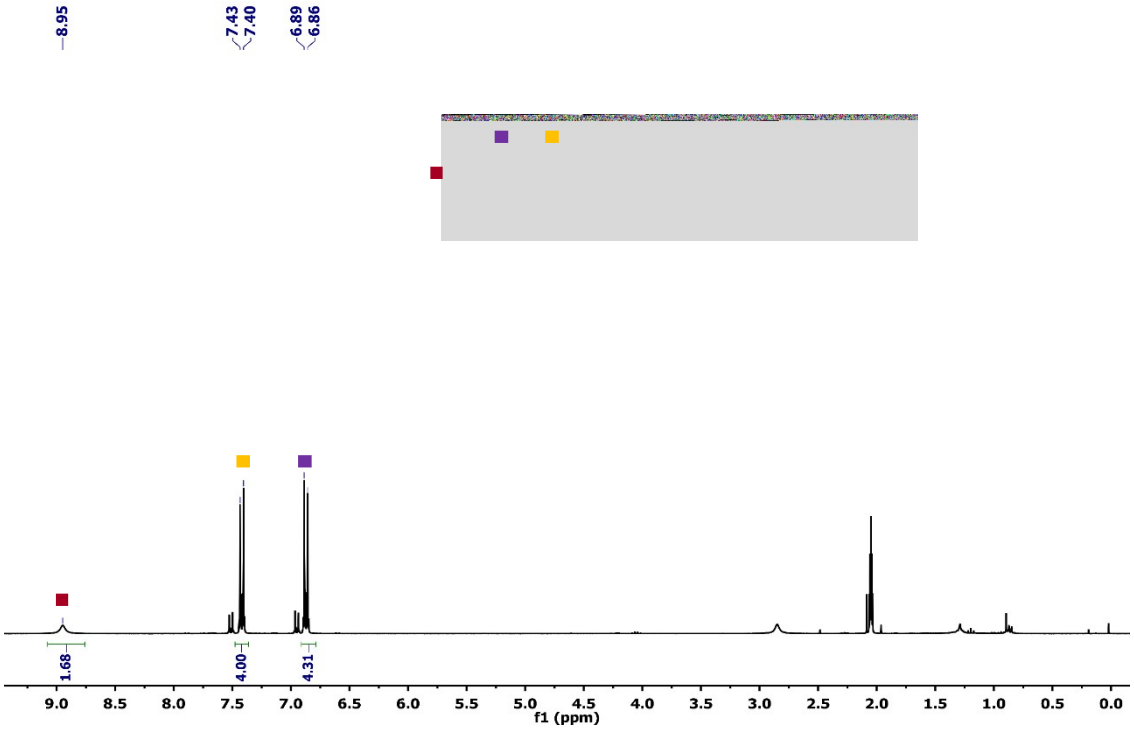

Figure S8. ^{1}H NMR spectrum (300 MHz, $CDCl_3$, 298K) of **OM5**

OM5 (^{13}C NMR, 300 MHz, $CDCl_3$, 298K)

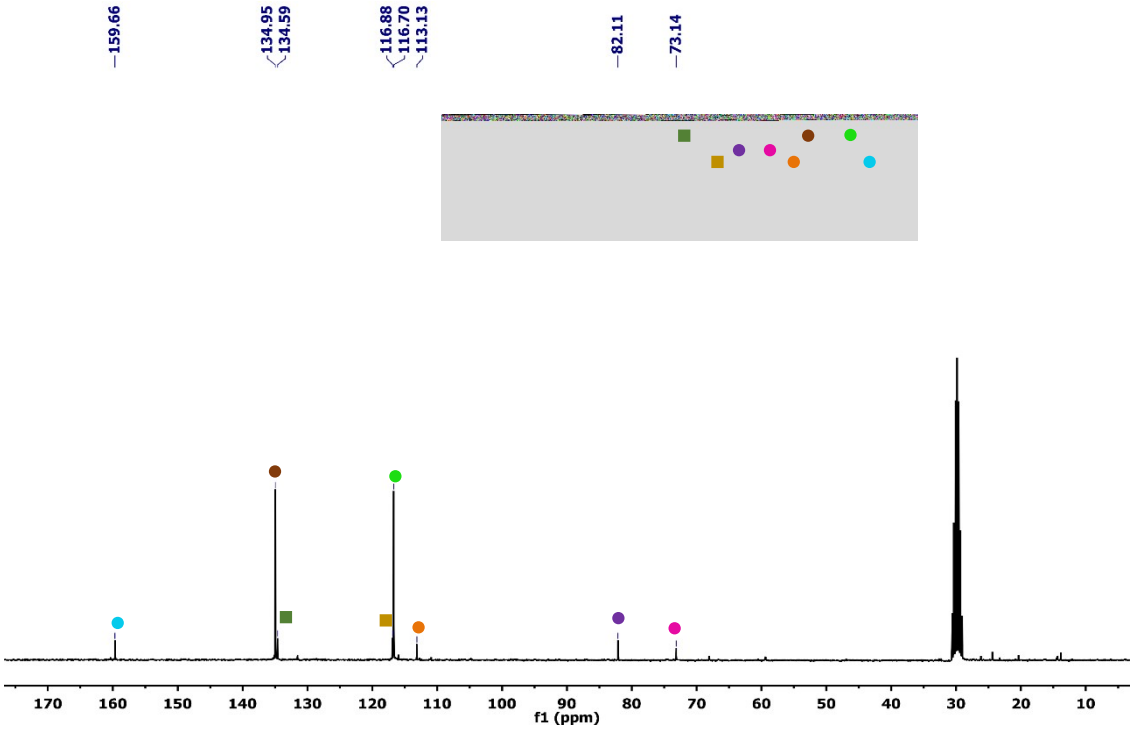

Figure S9. ^{13}C NMR spectrum (300 MHz, $CDCl_3$, 298K) of **OM5**

OM6 (^{1}H NMR, 300 MHz, $CDCl_3$, 298K)

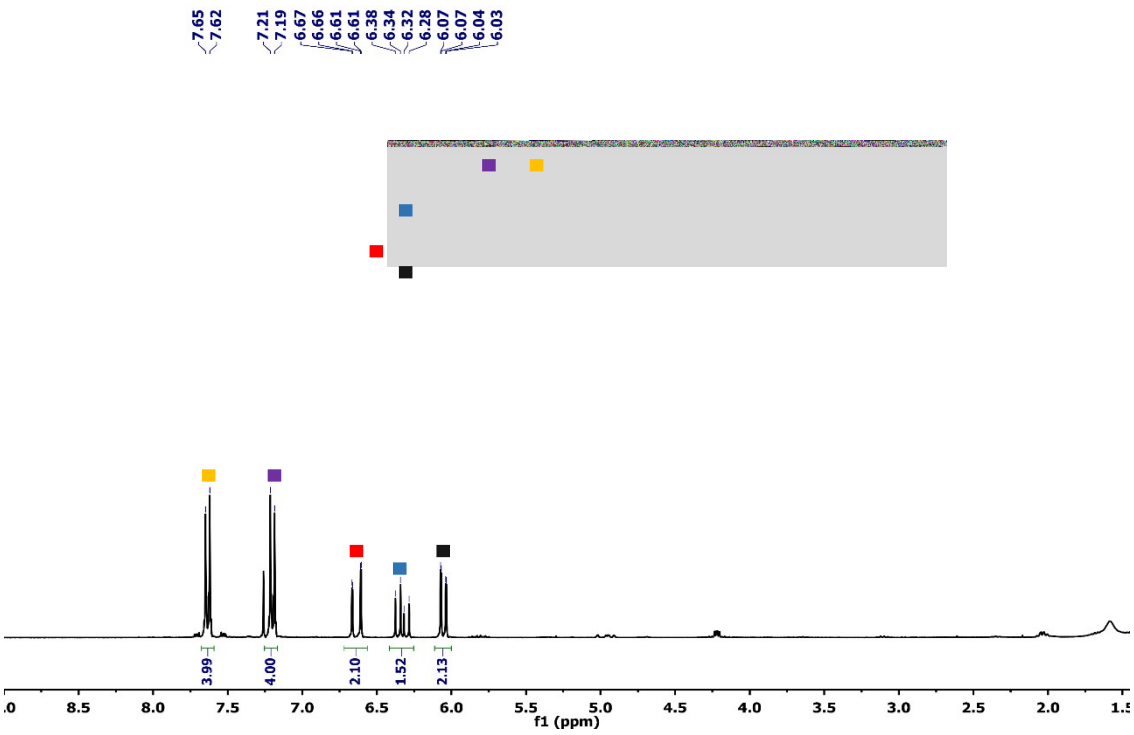

Figure S10. ^{1}H NMR spectrum (300 MHz, $CDCl_3$, 298K) of **OM6**

OM6 (^{13}C NMR, 300 MHz, $CDCl_3$, 298K)

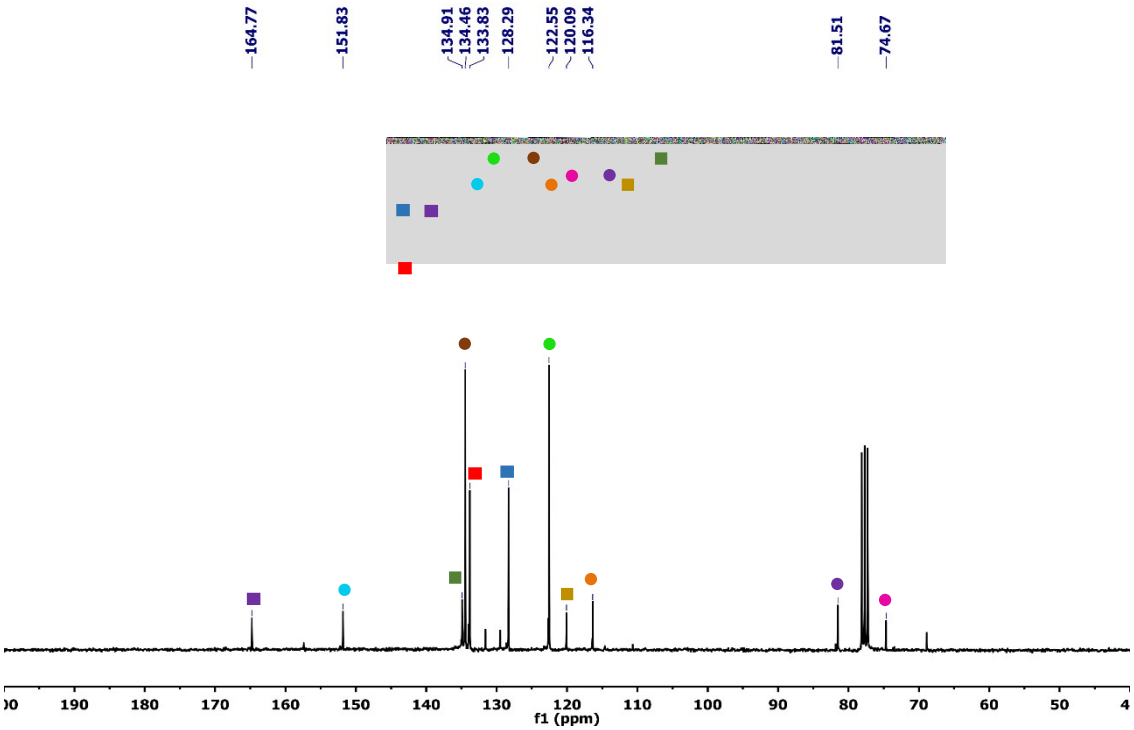

Figure S11. ^{13}C NMR spectrum (300 MHz, $CDCl_3$, 298K) of **OM6**

OM6 (^{19}F NMR, 300 MHz, $CDCl_3$, 298K)

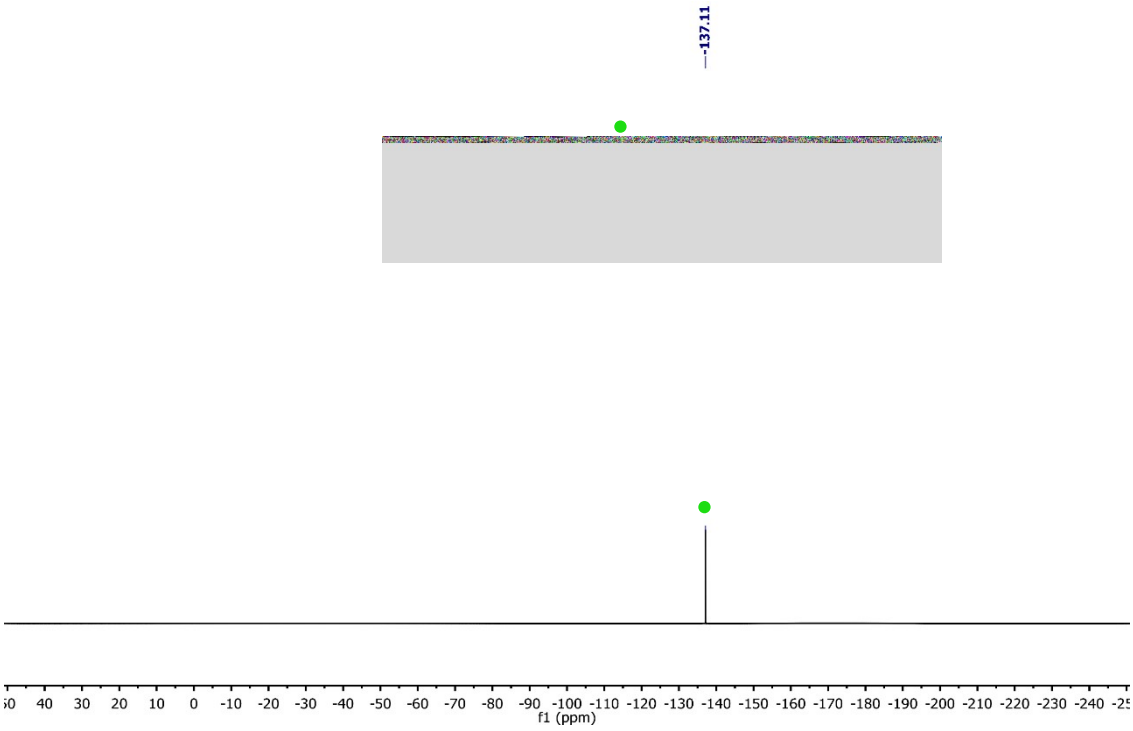

Figure S12. ^{19}F NMR spectrum (300 MHz, $CDCl_3$, 298K) of **OM6**

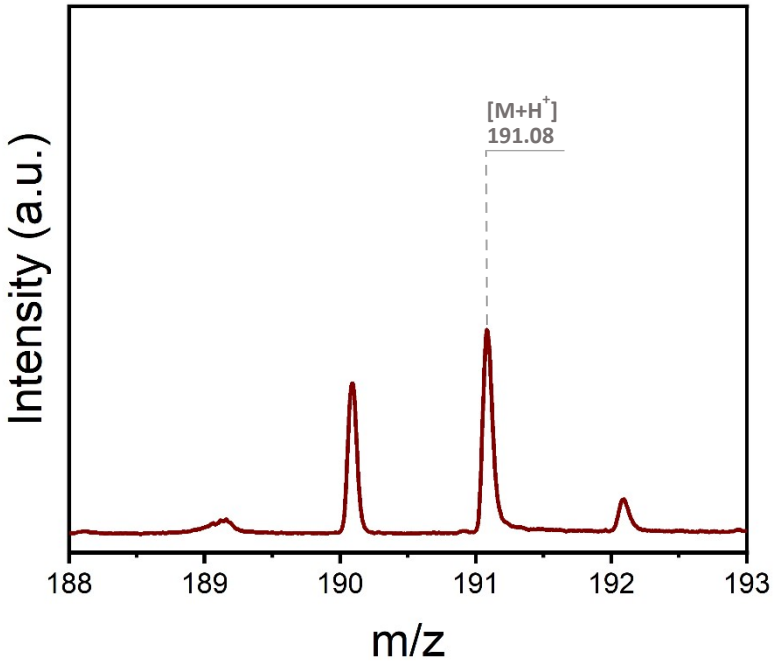

Figure S13. MALDI-TOF mass spectrum of **OM1**

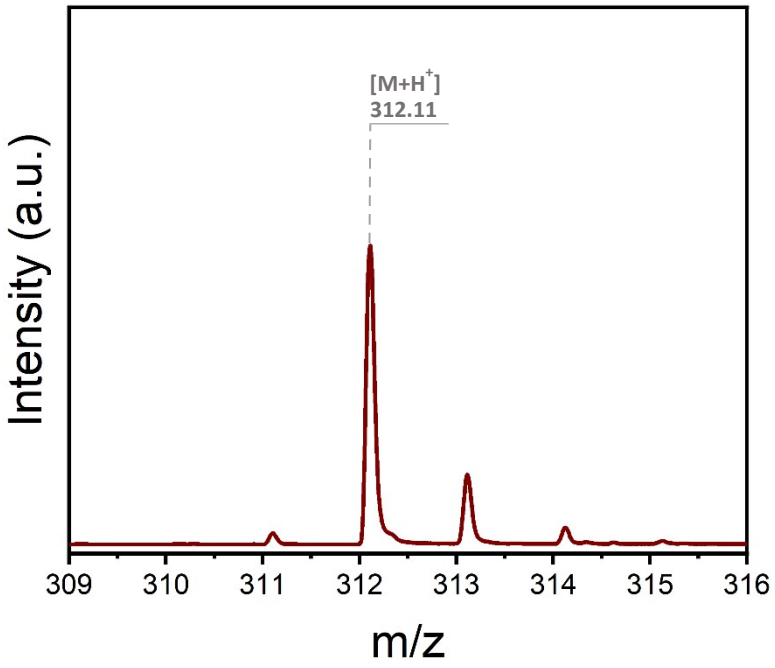

Figure S14. MALDI-TOF mass spectrum of **OM3**

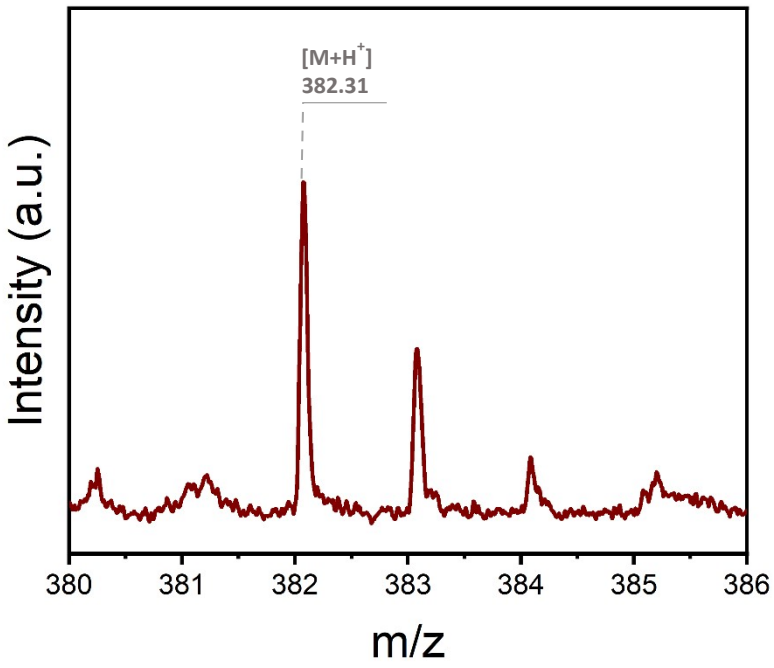

Figure S15. MALDI-TOF mass spectrum of **OM5**

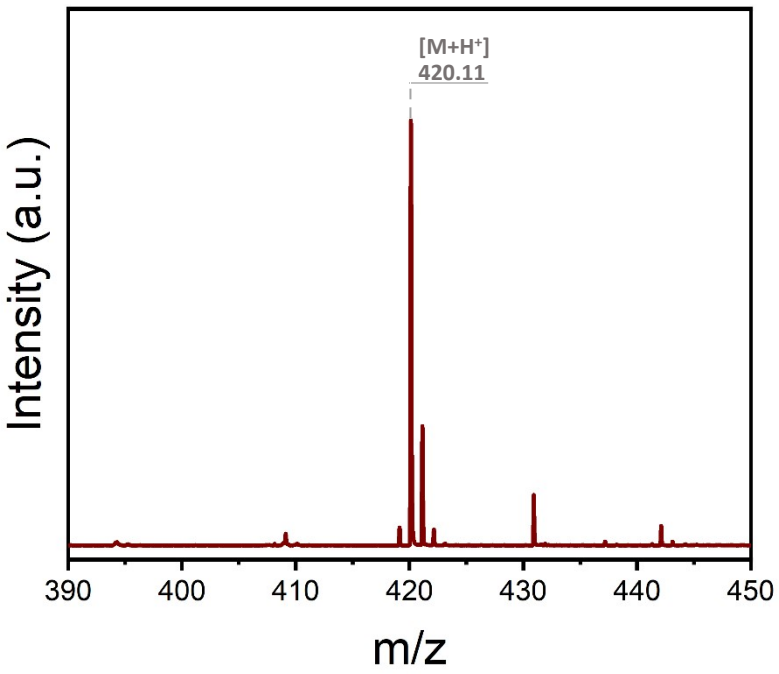

Figure S16 MALDI-TOF mass spectrum of **OM4**

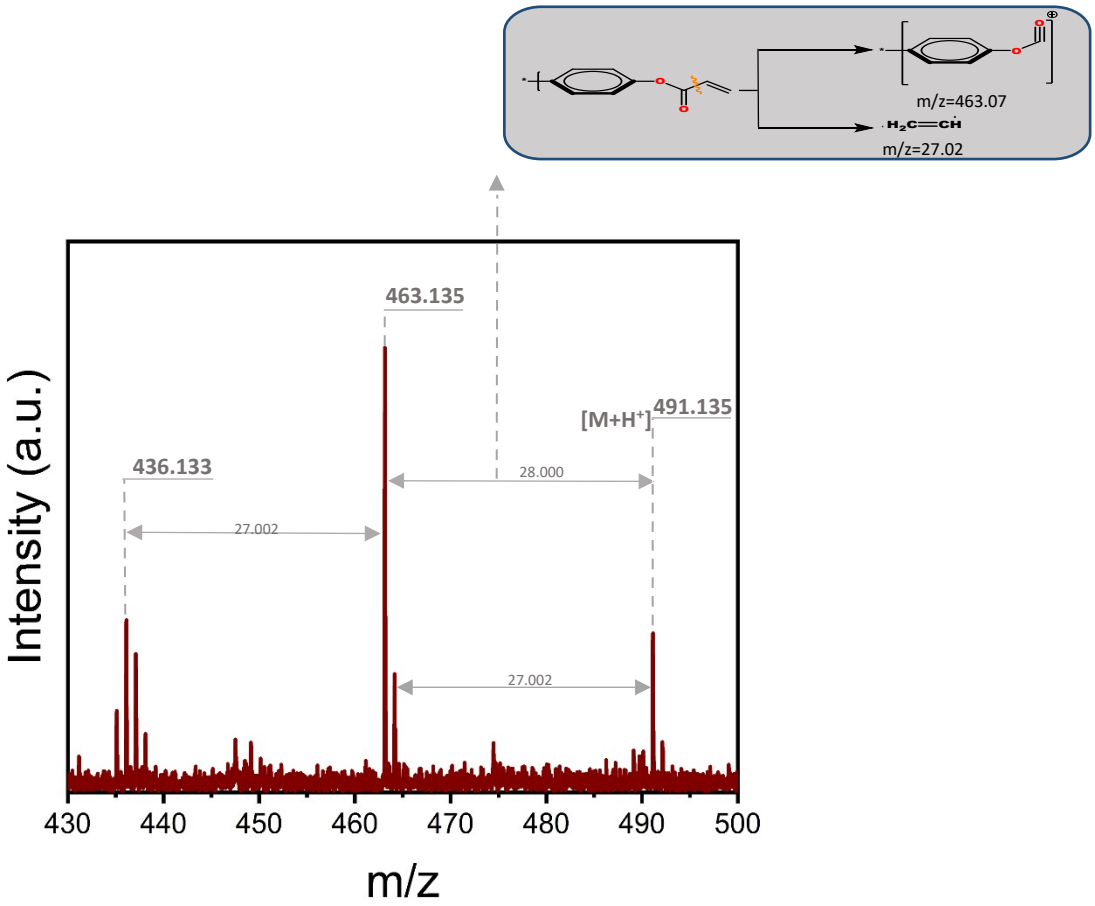

Figure S17 MALDI-TOF mass spectrum of **OM6**

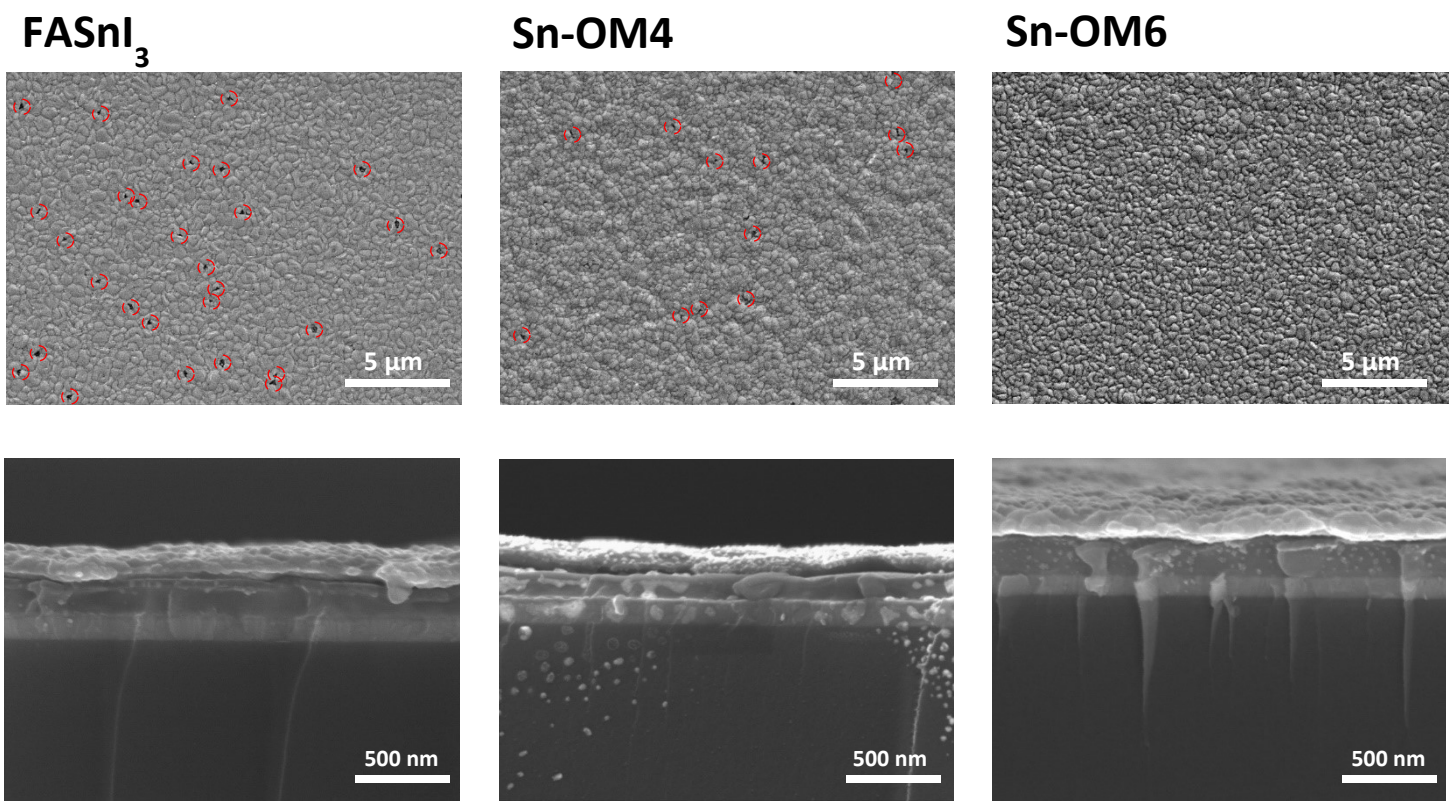

Figure S18. Top and cross section SEM images of perovskite films at top and bottom rows, respectively, with and without **OM4** and **OM6**, indicated in the column.

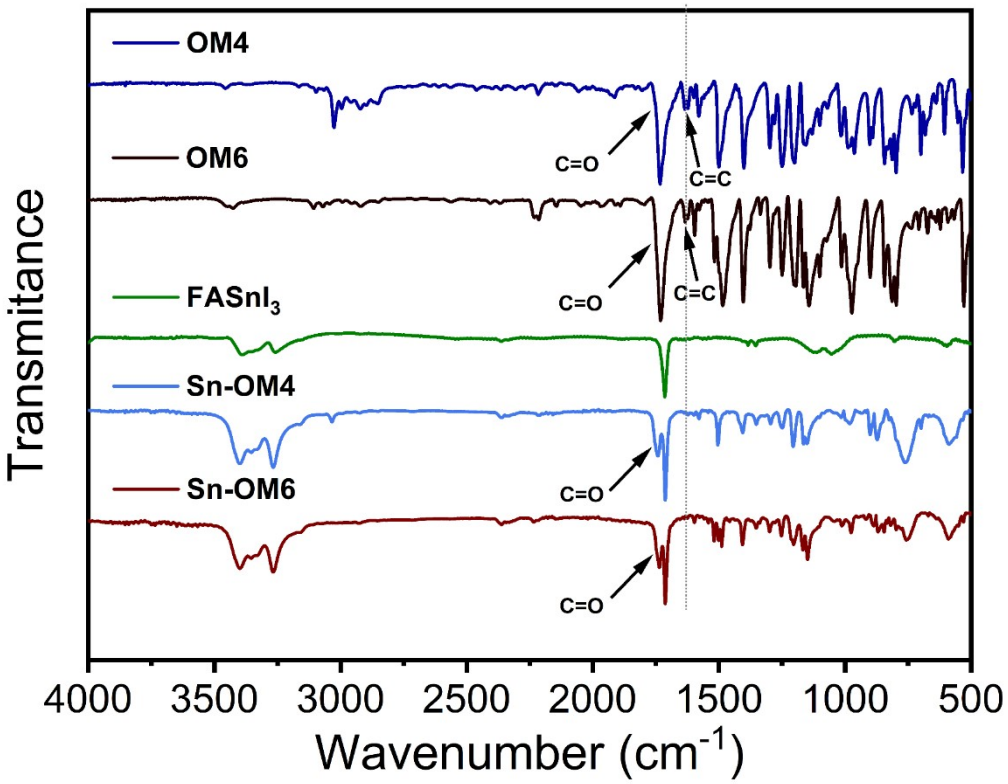

Figure S19. FTIR spectra for **OM4** and **OM6** molecules, as well as the pristine $FASnI_3$ perovskite film with and without additives.

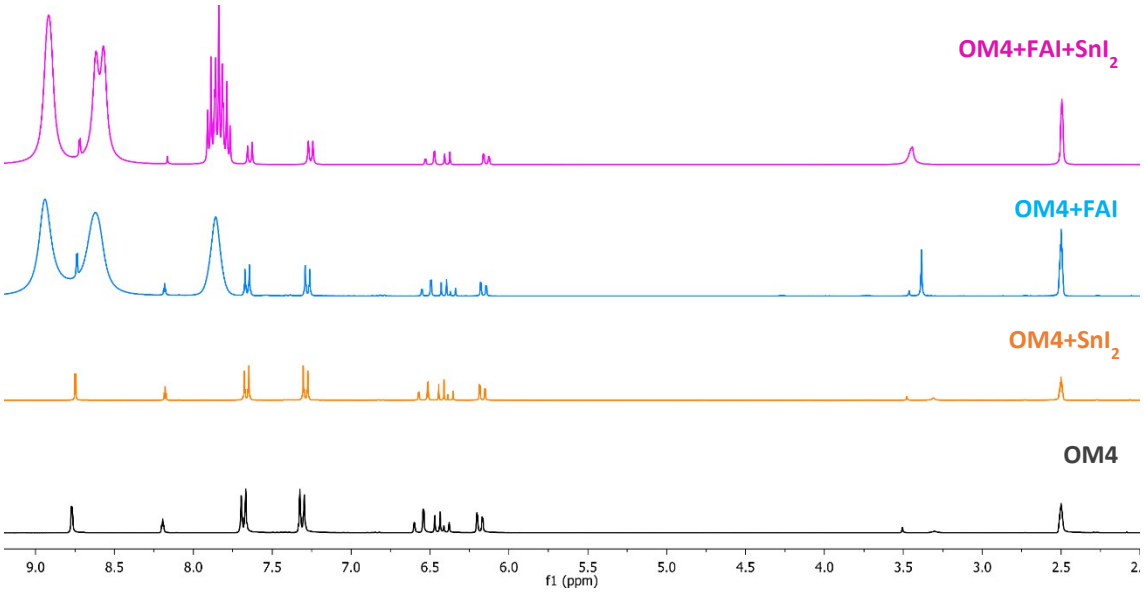

Figure S20. ^{1}H NMR spectra of **OM4**, **OM4**+SnI_2, **OM4**+FAI and **OM4**+FAI+SnI_2 in DMSO-d6.

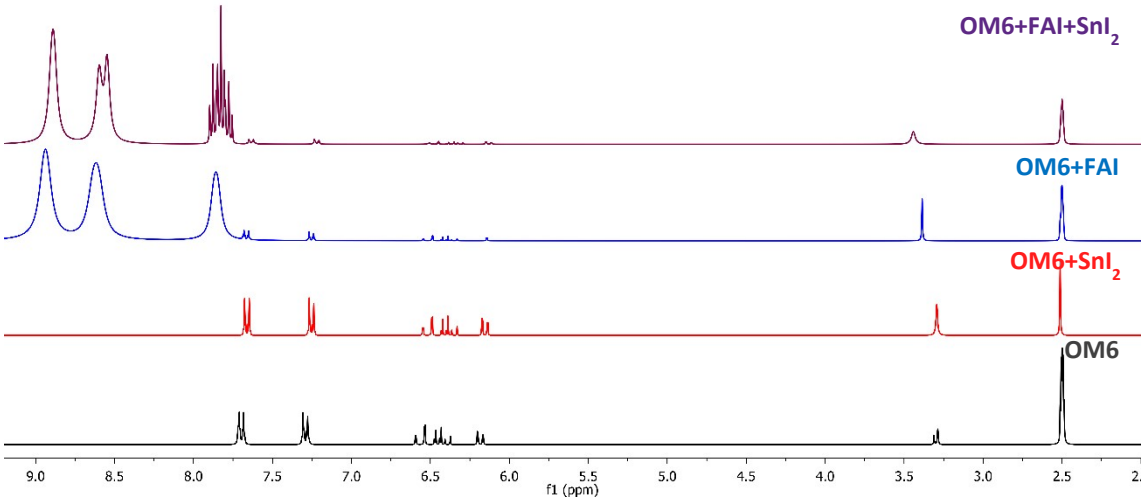

Figure S21. ^{1}H NMR spectra of **OM6**, **OM6**+SnI_2, **OM6**+FAI and **OM6**+FAI+SnI_2 in DMSO-d6.

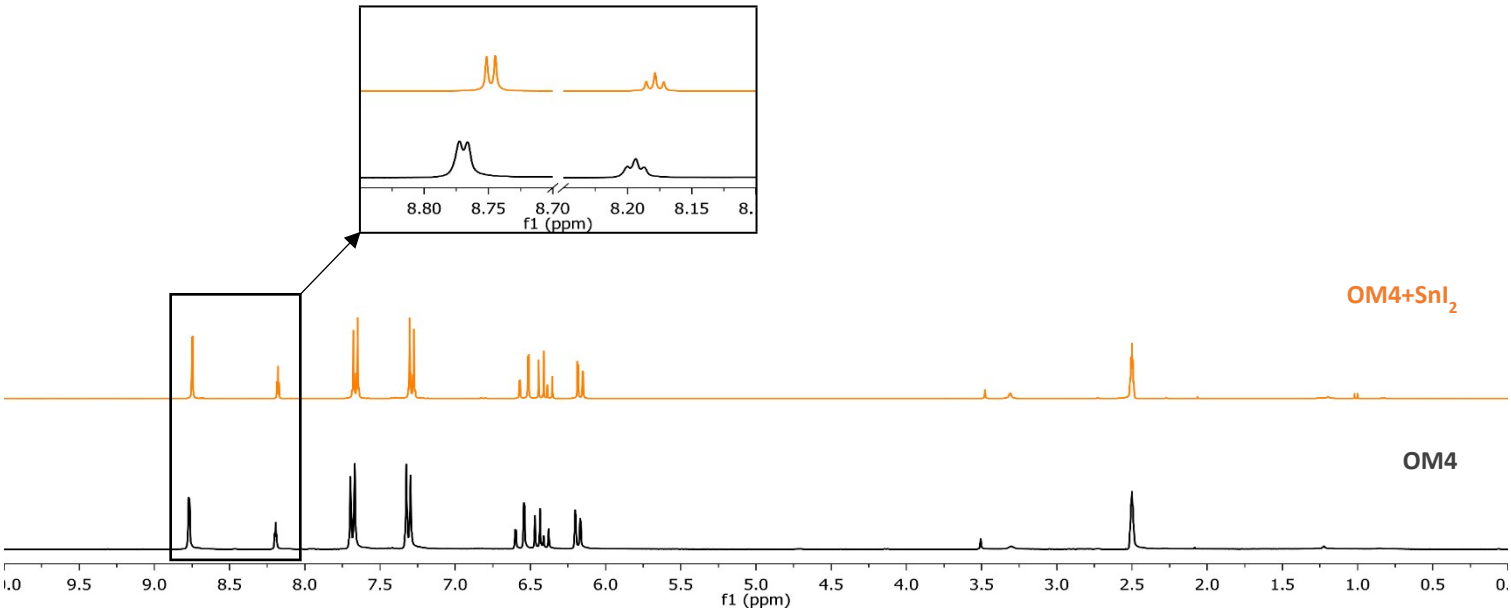

Figure S22. ^{1}H NMR spectra of **OM4** and **OM4**+SnI_2 DMSO-d6.

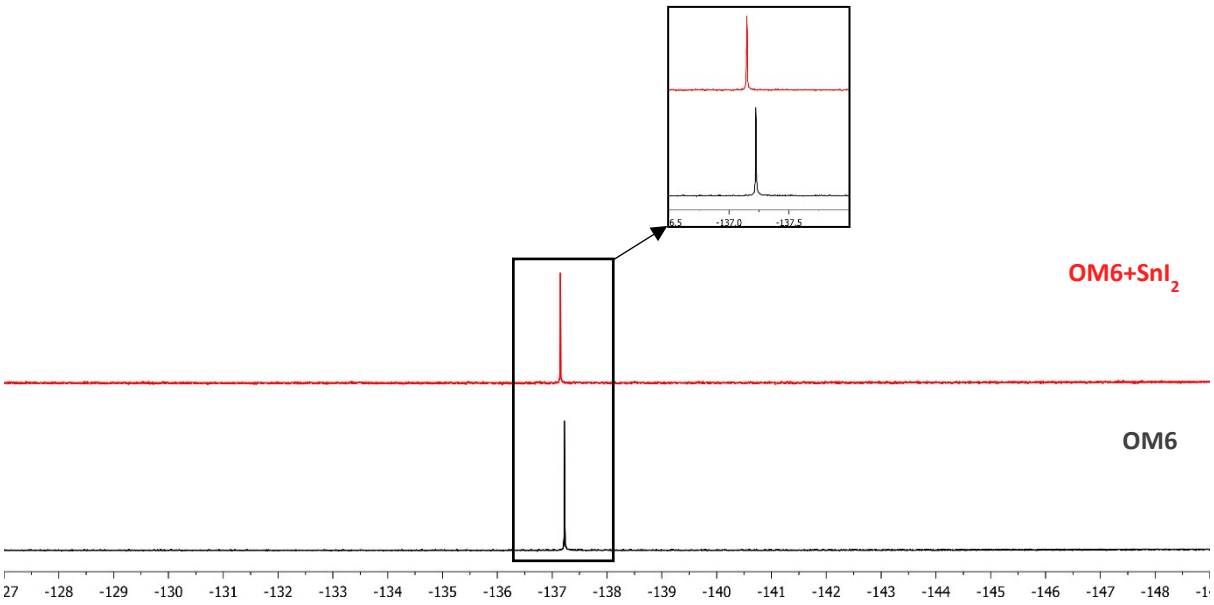

Figure S23. ^{19}F NMR spectra of **OM6** and **OM6**+SnI_2 DMSO-d6.

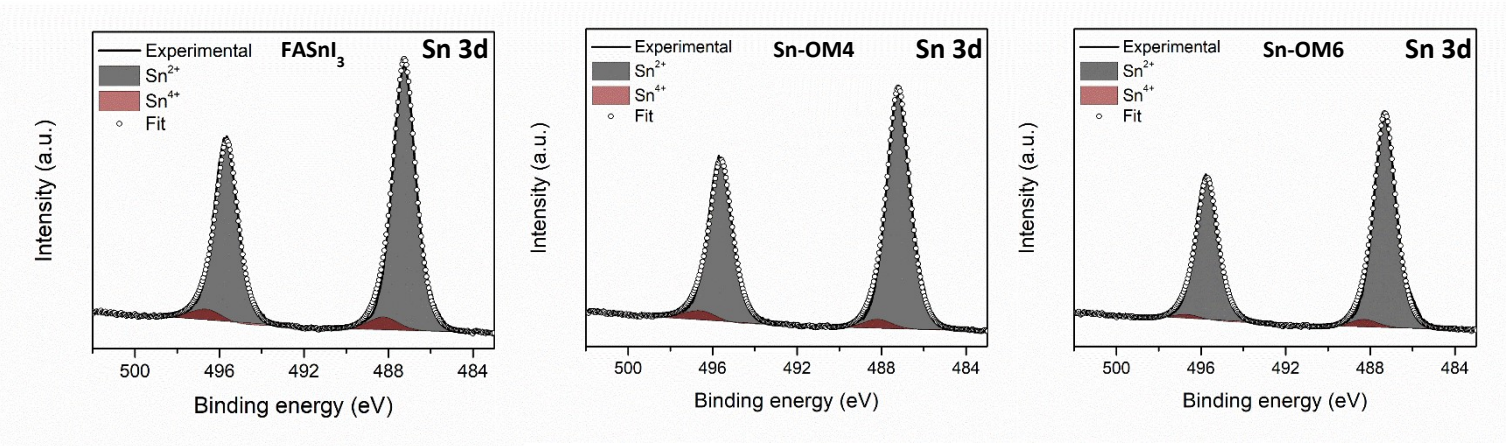

Figure S24. X-ray photoelectron spectroscopy spectra of Sn 3d for the perovskite films with and without **OM4** and **OM6**.

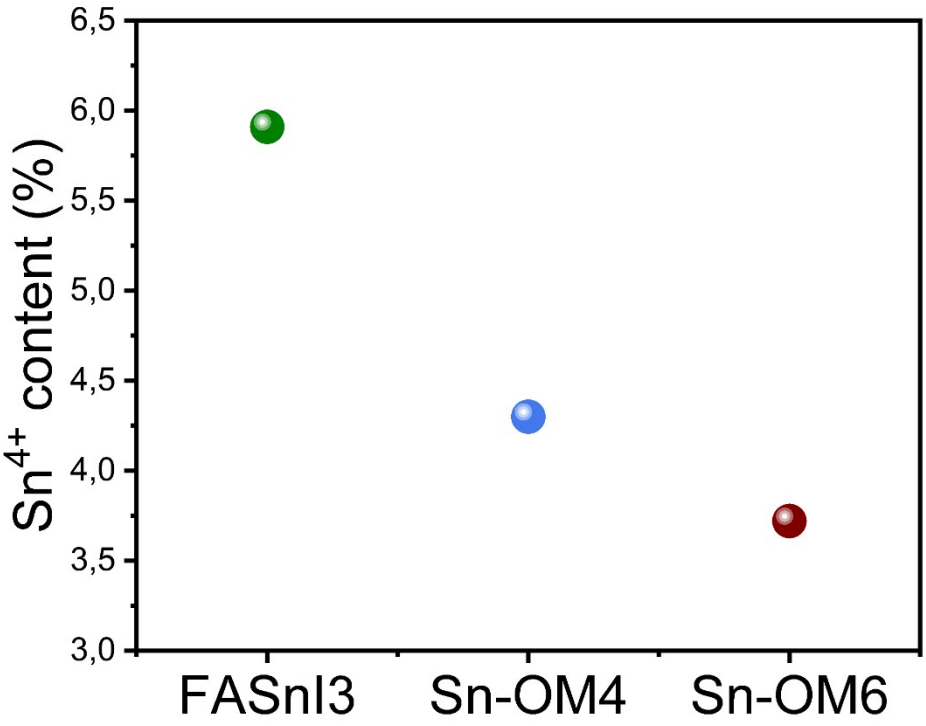

Figure S25. Variation in Sn^{4+} content (%) of pristine **$FASnI_3$**, **Sn-OM4** and **Sn-OM6** samples

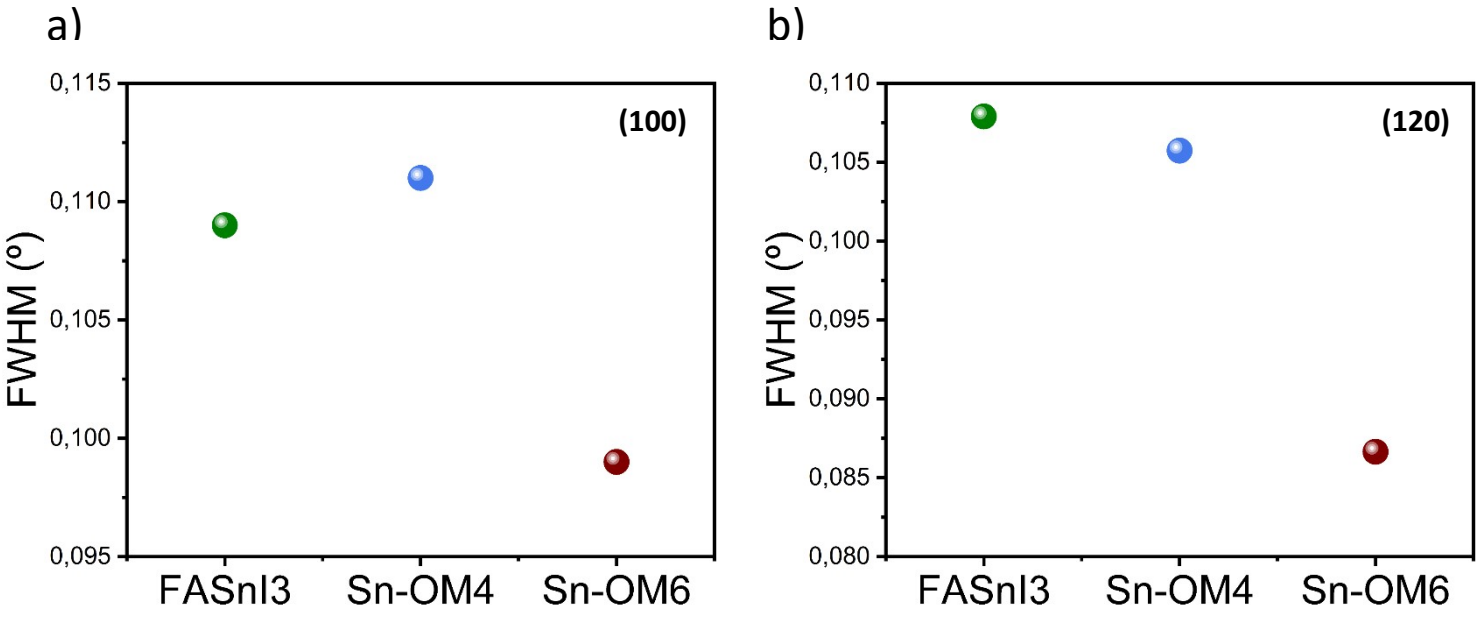

Figure S26. Full Width at Half-Maximum (FWHM) of the (a) (100) and (b) (120) diffraction peaks of **$FASnI_3$**, **Sn-OM4** and **Sn-OM6**.

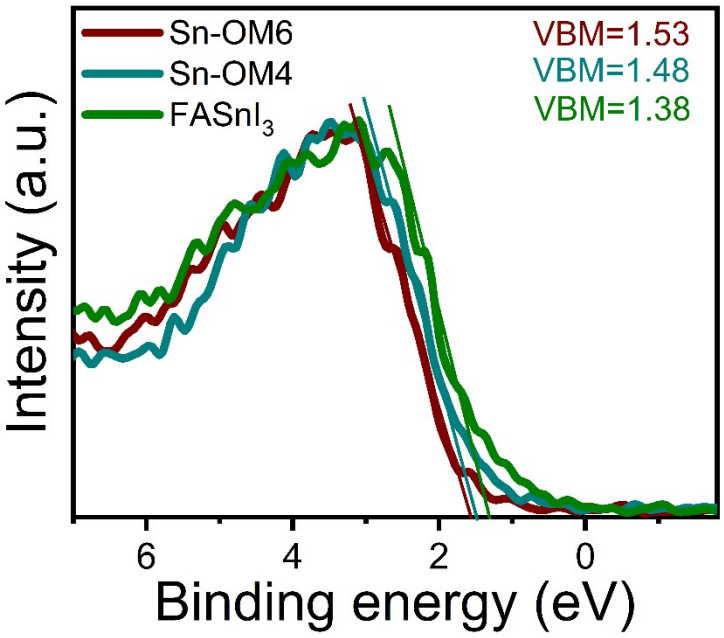

Figure S27. Valence band high resolution XPS spectra of the perovskite films with and without **OM4** and **OM6**.

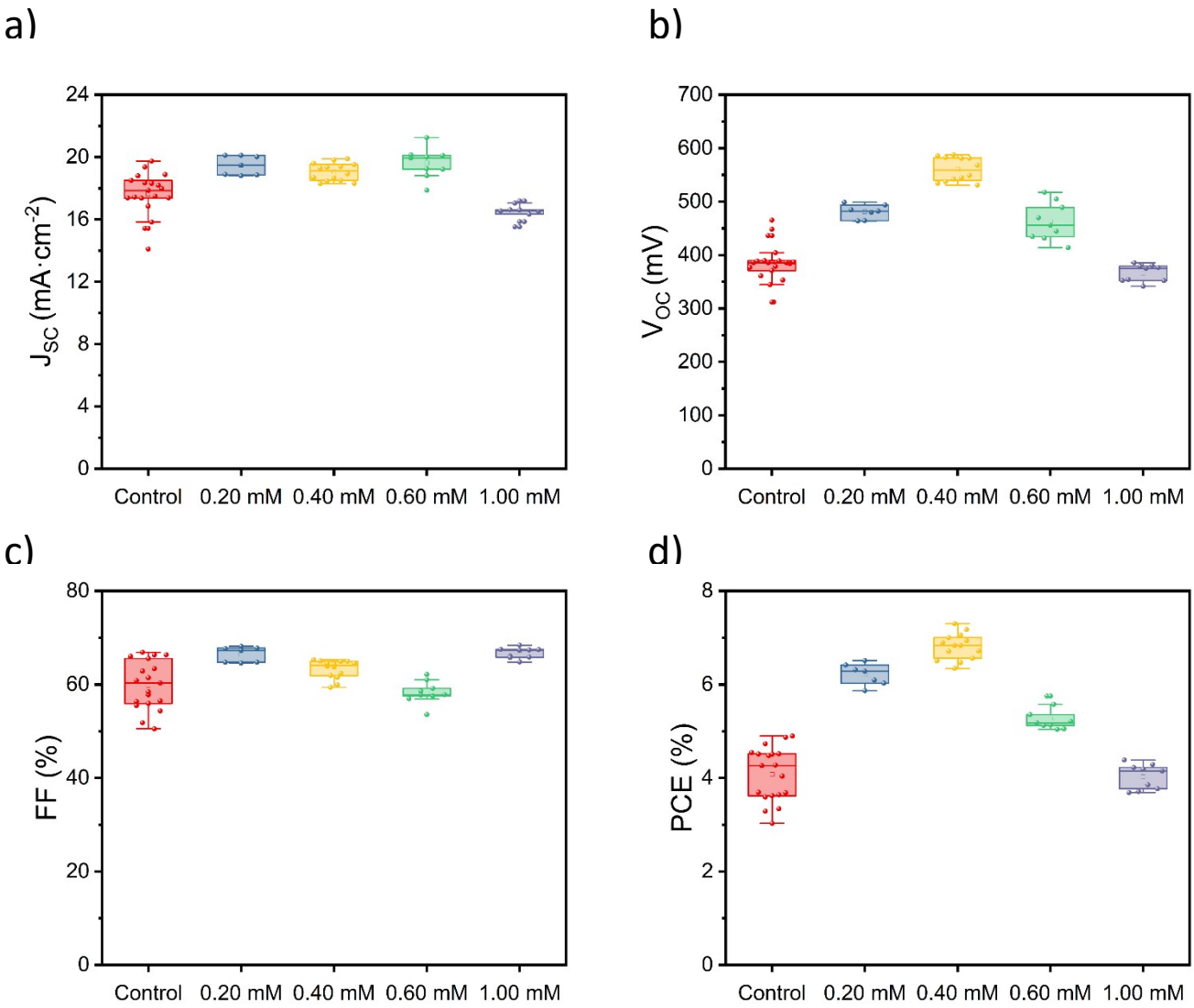

Figure S28. Statistics of the solar cell parameters with different concentrations of **OM4**: (a) J_{SC}, (b) V_{OC}, (c) FF and (d) PCE. All the parameters were extracted from J-V curves under 100 mW·cm^{-2} AM 1.5 G illumination.

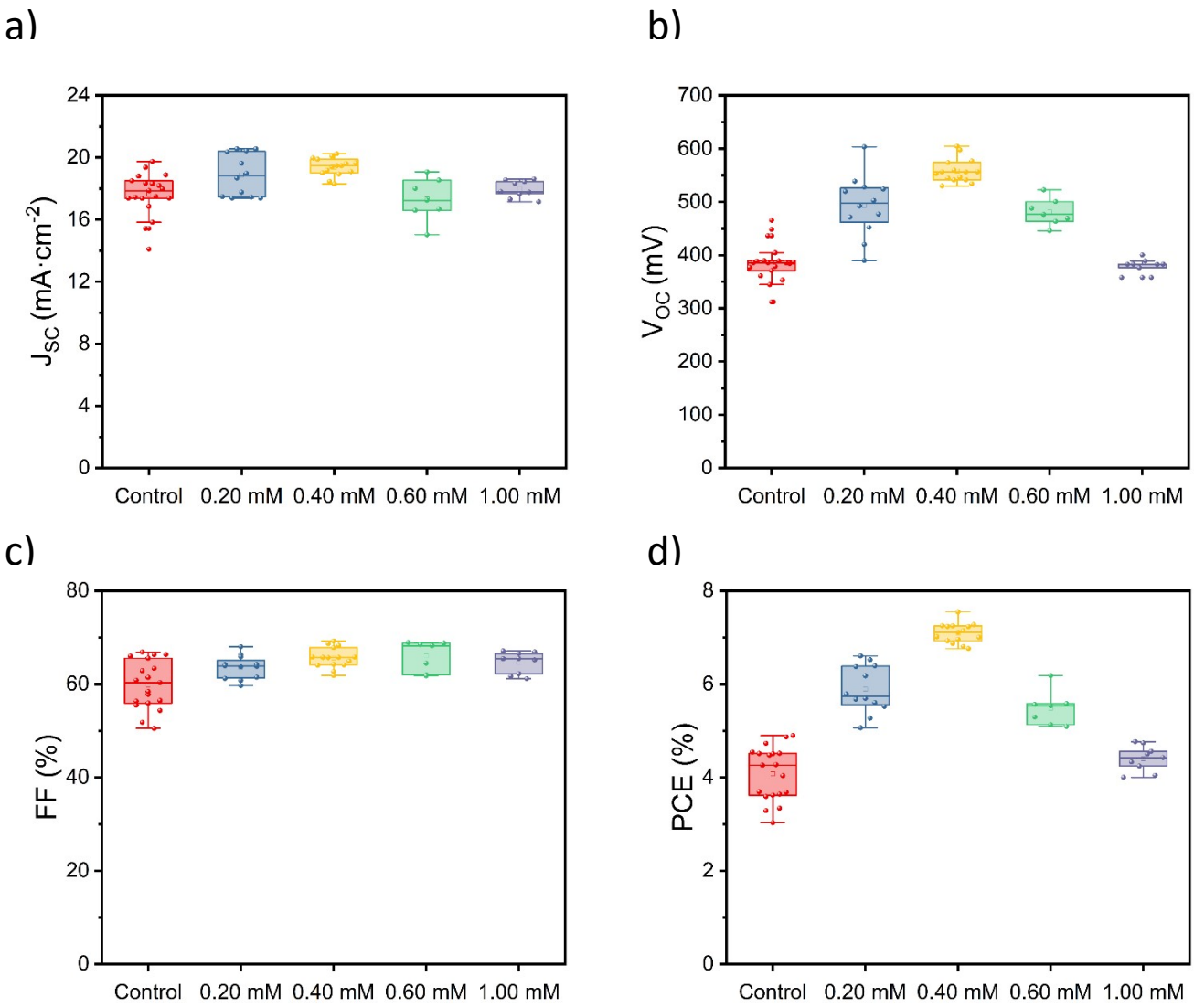

Figure S29. Statistics of the solar cell parameters with different concentrations of **OM6**: (a) J_{SC}, (b) V_{OC}, (c) FF and (d) PCE. All the parameters were extracted from J-V curves under 100 mW·cm^{-2} AM 1.5 G illumination.

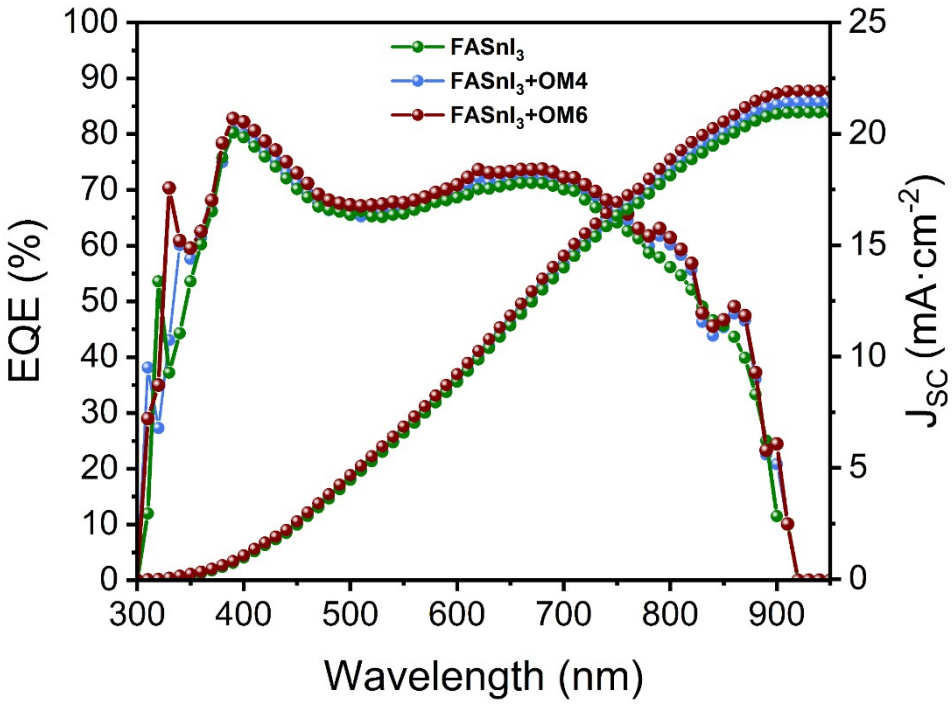

Figure S30. EQE spectrum and integrated current density of the devices with and without **OM4** and **OM6**.

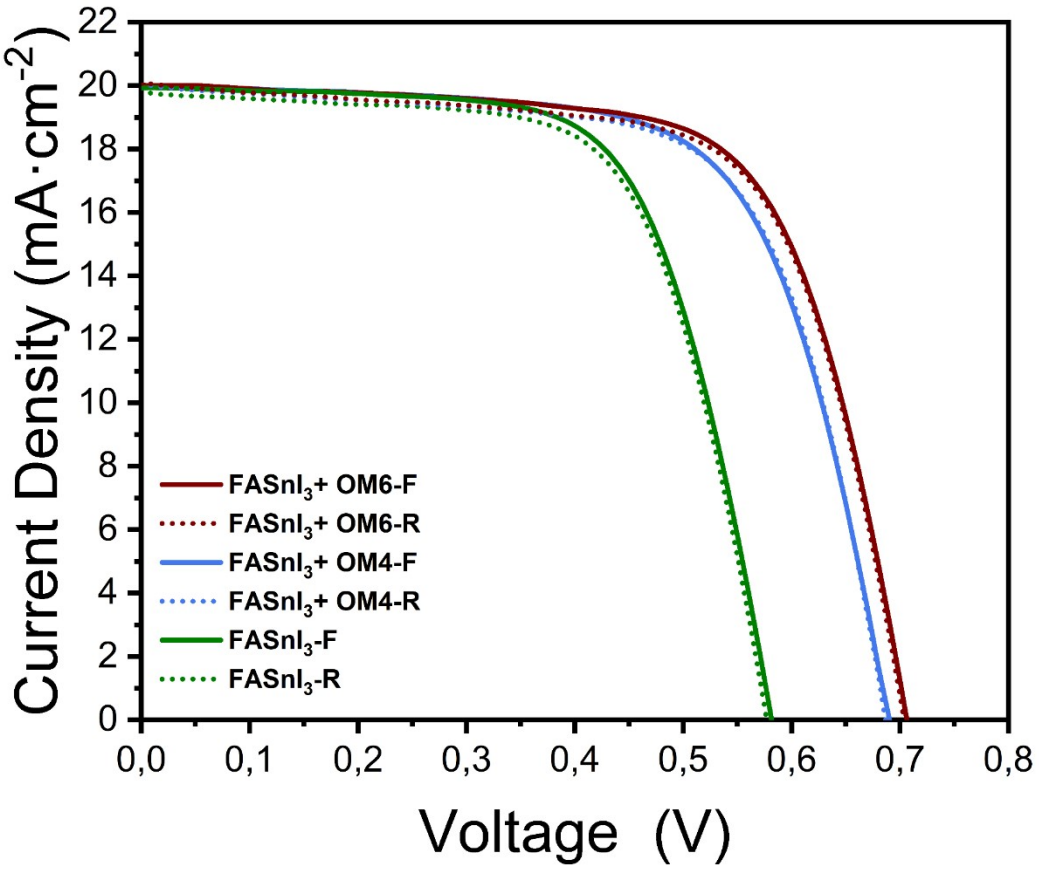

Figure S31. Forward (F) and reverse scans (R) of the J-V curves for the champion devices with and without **OM4** and **OM6**.

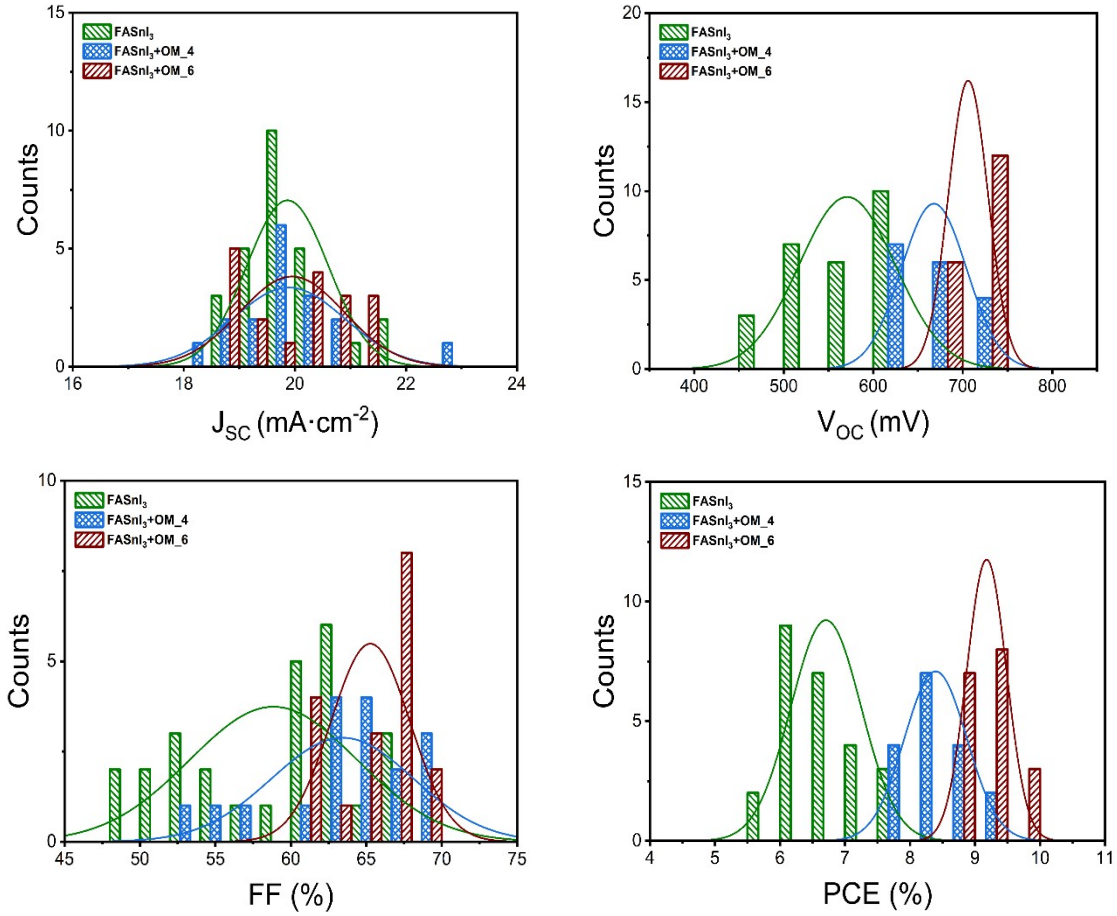

Figure S32. Device parameters histogram of 20 devices with and without **OM4** and **OM6** after the 3-days light-soaking treatment.

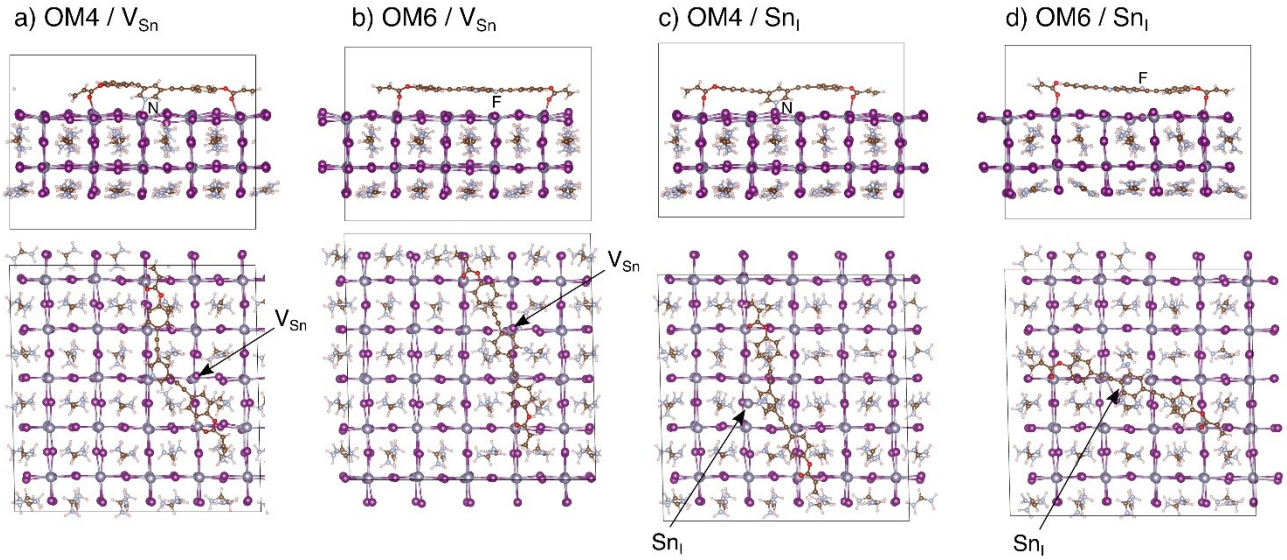

Figure S33. Atomic representation of $FASnI_3$ slabs with (001) surfaces including defects and ligands. Upper panels show side views, lower panels show top views.

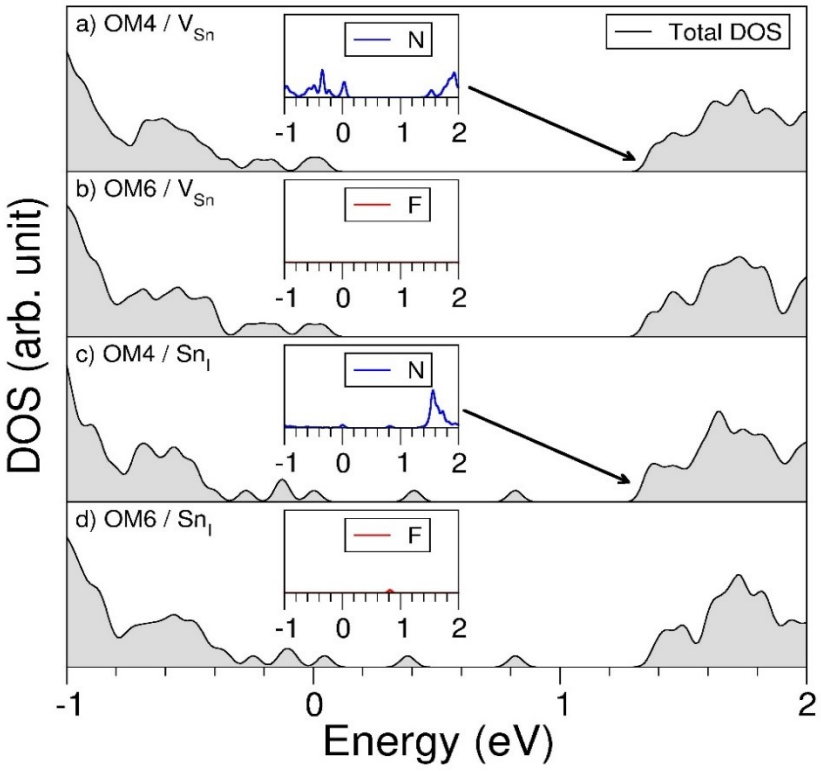

Figure S34. Band gap region with computed total DOS and projected DOS in the insets (only for spin up component). The arrows show the position of the peaks in the insets relative to the conduction band minima.

Table S1. Peak binding energies of $FASnI_3$, **Sn-OM4** and **Sn-OM6** films

	Binding Energy (eV)			
Sample	**Sn^{2+} ($3d_{3/2}$)**	**Sn^{4+} ($3d_{3/2}$)**	**Sn^{2+} ($3d_{5/2}$)**	**Sn^{4+} ($3d_{5/2}$)**
$FASnI_3$	495.79	496.79	487.39	488.39
Sn-OM4	495.71	496.71	487.31	488.31
Sn-OM6	495.65	496.65	487.25	488.25

Table S2. Decay times with the standard deviation deduced from TRPL spectra registered for the different films.

Sample	τ1 (ns)	A1	τ2 (ns)	A2	τave (ns)
$FASnI_3$	0.4	0.69	1.1	0.31	0.7
$FASnI_3$+OM4	1.3	0.88	2.8	0.12	1.4
$FASnI_3$+OM6	2.0	0.82	3.5	0.18	2.2

Table S3. Forward and reverse photovoltaic parameters of champion devices with each additive.

Sample	Scan direction	J_{SC} (mA·cm^{-2})	V_{OC} (V)	FF (%)	PCE (%)
$FASnI_3$	Forward	19.91	0.581	66.59	7.71
	Reverse	19.84	0.577	66.07	7.56
$FASnI_3$+OM4	Forward	19.97	0.689	67.14	9.25
	Reverse	20.13	0.686	66.89	9.24
$FASnI_3$+OM6	Forward	20.04	0.706	68.23	9.66
	Reverse	20.15	0.703	67.45	9.56

Table S4. Averaged photovoltaic parameters with the standard deviation for the devices with each additive.

Sample	J_{SC} (mA·cm^{-2})	V_{OC} (V)	FF (%)	PCE (%)
$FASnI_3$	19.9 ± 0.7	0.57 ± 0.05	59 ± 5	6.7 ± 0.5
$FASnI_3$+OM4	19.9 ± 1.0	0.67 ± 0.04	63 ± 5	8.4 ± 0.5
$FASnI_3$+OM6	19.9 ± 0.9	0.71 ± 0.02	65 ± 3	9.2 ± 0.3

Table S5. Summary of the best reported air-stability of FASnI3 based solar cells without encapsulation.

Device structure	Best PCE (%)	Storage condition	Lifetime (80% retention)	Ref
FTO/(PEG)PEDOT:PSS/$FASnI_3$/PCBM/BCP/Ag	5.12	Dark, 40% RH	6 h	[9]
ITO/PEDOT:PSS/GUA:$FASnI_3$/C60/BCP/Ag	9.60	Dark, 60% RH	96 h	[10]
ITO/NiOx/$FASnI_3$ (KHQSA)/PCBM/Ag	6.76	Dark, 20% RH	500 h	[11]
ITO/NiOx/$FASnI_3$ (GA)/PCBM/ BCP/Ag	9.03	Dark, 20% RH	1000 h	[12]
ITO/PEDOT:PSS/ $FASnI_3$ (3D/2D)/C_{60}/BCP/Ag	10.60	Dark, 40% RH	240 h	[13]
ITO/PEDOT:PSS/$FASnI_3$ (MACl)/PCBM/Al	7.14	Dark, 37% RH	4 h	[14]
ITO/PEDOT:PSS/$FASnI_3$ ($C_{60}Cl_6$)/PCBM/BCP/Ag	13.30	Dark, 20% RH	10h*	[15]
ITO/PEDOT:PSS/$MAFASnI_{2.75}Br_{0.25}$/PCBM/BCP/Ag	10.30	Dark, 40% RH	30 h	[16]
ITO/PEDOT:PSS/$FASnI_{2.7}Br_{0.3}$/PCBM/PDINN/Cu	13.05	Dark, 20% RH	8 h	[17]
ITO/PEDOT:PSS/$FASnI_3$ (OM4)/C_{60}/BCP/Ag	9.25	Dark, 30% RH	220 h	This Work
ITO/PEDOT:PSS/$FASnI_3$ (OM6)/C_{60}/BCP/Ag	9.66	Dark, 30% RH	250 h**	This Work

*95% retention after 10 hours
**>90% retention after 250 hours

1. Sanchez-Diaz, J.; Sánchez, R. S.; Masi, S.; Krecmarová, M.; Alvarez, A. O.; Barea, E. M.; Rodriguez-Romero, J.; Chirvony, V. S.; Sánchez-Royo, J. F.; Martinez-Pastor, J. P.; Mora-Seró, I., Tin perovskite solar cells with >1,300 h of operational stability in N2 through a synergistic chemical engineering approach. *Joule* **2022,** *6* (4), 861-883.
2. Jiang, Y.; Lu, Z.; Zou, S.; Lai, H.; Zhang, Z.; Luo, J.; Huang, Y.; He, R.; Jin, J.; Yi, Z.; Luo, Y.; Wang, W.; Wang, C.; Hao, X.; Chen, C.; Wang, X.; Wang, Y.; Ren, S.; Shi, T.; Fu, F.; Zhao, D., Dual-site passivation of tin-related defects enabling efficient lead-free tin perovskite solar cells. *Nano Energy* **2022,** *103*, 107818.
3. Kresse, G.; Hafner, J., Ab initio molecular-dynamics simulation of the liquid-metal--amorphous-semiconductor transition in germanium. *Physical Review B* **1994,** *49* (20), 14251-14269.
4. Kresse, G.; Furthmüller, J., Efficiency of ab-initio total energy calculations for metals and semiconductors using a plane-wave basis set. *Computational Materials Science* **1996,** *6* (1), 15-50.
5. Kresse, G.; Hafner, J., Ab initio molecular dynamics for liquid metals. *Physical Review B* **1993,** *47* (1), 558-561.
6. Kresse, G.; Furthmüller, J., Efficient iterative schemes for ab initio total-energy calculations using a plane-wave basis set. *Physical Review B* **1996,** *54* (16), 11169-11186.
7. Perdew, J. P.; Burke, K.; Ernzerhof, M., Generalized Gradient Approximation Made Simple. *Physical Review Letters* **1996,** *77* (18), 3865-3868.
8. Grimme, S.; Antony, J.; Ehrlich, S.; Krieg, H., A consistent and accurate ab initio parametrization of density functional dispersion correction (DFT-D) for the 94 elements H-Pu. *The Journal of Chemical Physics* **2010,** *132* (15).
9. Liu, X.; Wang, Y.; Xie, F.; Yang, X.; Han, L., Improving the Performance of Inverted Formamidinium Tin Iodide Perovskite Solar Cells by Reducing the Energy-Level Mismatch. *ACS Energy Letters* **2018,** *3* (5), 1116-1121.
10. Jokar, E.; Chien, C.-H.; Tsai, C.-M.; Fathi, A.; Diau, E. W.-G., Robust Tin-Based Perovskite Solar Cells with Hybrid Organic Cations to Attain Efficiency Approaching 10%. **2019,** *31* (2), 1804835.
11. Tai, Q.; Guo, X.; Tang, G.; You, P.; Ng, T.-W.; Shen, D.; Cao, J.; Liu, C.-K.; Wang, N.; Zhu, Y.; Lee, C.-S.; Yan, F., Antioxidant Grain Passivation for Air-Stable Tin-Based Perovskite Solar Cells. **2019,** *58* (3), 806-810.
12. Wang, T.; Tai, Q.; Guo, X.; Cao, J.; Liu, C.-K.; Wang, N.; Shen, D.; Zhu, Y.; Lee, C.-S.; Yan, F., Highly Air-Stable Tin-Based Perovskite Solar Cells through Grain-Surface Protection by Gallic Acid. *ACS Energy Letters* **2020,** *5* (6), 1741-1749.
13. Jokar, E.; Cheng, P.-Y.; Lin, C.-Y.; Narra, S.; Shahbazi, S.; Wei-Guang Diau, E., Enhanced Performance and Stability of 3D/2D Tin Perovskite Solar Cells Fabricated with a Sequential Solution Deposition. *ACS Energy Letters* **2021,** *6* (2), 485-492.
14. Yang, S. J.; Choi, J.; Song, S.; Park, C.; Cho, K., Enhancing air-stability and reproducibility of lead-free formamidinium-based tin perovskite solar cell by chlorine doping. *Solar Energy Materials and Solar Cells* **2021,** *227*, 111072.
15. Chen, J.; Tian, C.; Sun, C.; Yang, P.; Feng, W.; Zheng, L.; Yang, L.; Hou, E.; Luo, J.; Xie, L.; Wei, Z., Chlorofullerene C60Cl6 Enables Efficient and Stable Tin-Based Perovskite Solar Cells. **2022,** *7* (1), e12529.

16. Liu, J.; Wang, S.; Zhu, W.; Tang, Z.; Ding, L.; Hao, F., Highly symmetric Lewis base coordinated with Sn2+ for reducing voltage loss and retarding oxidation in tin-halide perovskite solar cells. *Chemical Engineering Journal* **2023,** *453*, 139975.
17. Obila, J. O.; Ryu, D. H.; Oh, S.; Kim, J. H.; Musembi, R. J.; Lee, S.; Kang, B. J.; Jeon, N. J.; Ayieta, E. O.; Im, S. H.; Song, C. E., Tin-Based Perovskite Solar Cells Containing a Perylene Diimide Cathode Interlayer with a Copper Top Electrode. *ACS Energy Letters* **2024,** *9* (3), 1090-1096.